Supporting Information

Stabilization of Super Electrophilic Pd^{+2} Cations in Small-pore SSZ-13 Zeolite

Konstantin Khivantsev[1§*], Nicholas R. Jaegers[1,2§], Iskra Z. Koleva[3§], Hristiyan A. Aleksandrov[3*], Libor Kovarik[1], Mark Engelhard[1], Feng Gao,[1] Yong Wang[1,2], Georgi N. Vayssilov[3], and Janos Szanyi[1*]

[1]Institute for Integrated Catalysis, Pacific Northwest National Laboratory Richland, WA 99352 USA

[2]Voiland School of Chemical Engineering and Bioengineering, Washington State University, Pullman, WA 99163 USA

[3]Faculty of Chemistry and Pharmacy, University of Sofia, 1126 Sofia, Bulgaria

*corresponding authors: KK: Konstantin.Khivantsev@pnnl.gov, HAA: Haa@chem.uni-sofia.bg and JSz: Janos.Szanyi@pnnl.gov

§ these authors contributed equally KK, NRJ, IZK, JSz

Methods

Na-SSZ-13 with Si/Al = 6 and ion-exchanged twice with 2 M NH_4NO_3 aqueous solution at 80 °C for 3 hours yielding the ammonium forms of SSZ-13. NH_4-SSZ-13 was subsequently dried under ambient conditions and then at 80 ºC. Samples with 0.1 and 1 wt% Pd, 1 wt% Pt and 3 wt% Ag loadings were prepared by modified ion exchange (for Pd and Pt) with 10 wt% $Pd(NH_3)_4(NO_3)_2$ solution (Sigma-Aldrich 99.99%) with NH_4-SSZ-13, and platinum(II) tetraamine nitrate solution, and regular ion exchange for $AgNO_3$ (99.99%) solution with H-SSZ-13 (produced by decomposition of NH_4-SSZ-13 in air at 550 °C). More specifically, minimum amount of the Pd(II) or Pt(II) precursor solution was added to zeolite in the amount approximately equivalent to the total pore volume of the zeolite. The thick paste was mixed and stirred vigorously for 30 minutes, followed by calcination in air at 650 °C for 5 h (ramping rate 2 °C/min) in case of Pd and 350°C in case of Pt. H-forms of zeolites could be used as well with identical results: in that case, Pd and Pt tetramine salts were dissolved in the minimum amount of dilute ammonium hydroxide solution (pH=11.5), mixed with zeolite to form thick paste (mixed vigorously), followed by drying and calcination in air at 650 °C for Pd and 350 °C for Pt. In the case of Ag, 1 g of H-SSZ-13 was dispersed in water and stirred with ~20 ml of 0.1 M silver nitrate solution for 3 hours; then the sample was purified by 5 successive centrifugation-redispersion cycles and dried at 80 ºC overnight. To avoid silver auto-reduction under high vacuum in the FTIR cell, the sample was heated to 180 °C to remove residual water from Ag/SSZ-13 as quickly as possible and then immediately cooled down prior to IR measurements.

The in situ static transmission IR experiments were conducted in a home-built cell housed in the sample compartment of a Bruker Vertex 80 spectrometer, equipped with an MCT detector and operated at 4 cm^{-1} resolution. The powder sample was pressed onto a tungsten mesh which, in turn, was mounted onto a copper heating assembly attached to a ceramic feedthrough. The sample could be resistively heated, and the sample temperature was monitored by a thermocouple spot welded onto the top center of the W grid. The cold finger on the glass bulb containing CO was cooled with liquid nitrogen to eliminate any contamination originating from metal carbonyls, while NO was cleaned with multiple freeze–pump–thaw cycles. Prior to spectrum collection, a background

with the activated (annealed, reduced or oxidized) sample in the IR beam was collected. Each spectrum reported is obtained by averaging 256 scans.

HAADF-STEM was used to probe the dispersion of Pd and Pt in prepared samples. The analysis was performed with a FEI Titan 80-300 microscope operated at 300 kV. The instrument is equipped with a CEOS GmbH double-hexapole aberration corrector for the probe-forming lens, which allows for imaging with 0.1 nm resolution in scanning transmission electron microscopy mode (STEM). The images were acquired with a high angle annular dark field (HAADF) detector with inner collection angle set to 52 mrad.

Standard NOx adsorption tests were conducted in a plug-flow reactor system with powder samples (120 mg, 60–80 mesh) loaded in a quartz tube, using a synthetic gas mixture that contained ~200 ppm of NOx or (200 ppm of NOx, 200 ppm CO, 3 vw% H_2O and 14% O_2) balanced with N_2 at a flow rate of 310 sccm (corresponding to 330,000 h^{-1}).

All the gas lines were heated to over 100 °C. Concentrations of reactants and products were measured by an online MKS MultiGas 2030 FTIR gas analyzer with a gas cell maintained at 191 °C. Two four-way valves were used for gas switching between the reactor and the bypass. Prior to storage testing at 100 °C, the sample was pretreated in 14% O_2 balanced in N_2 flow for 1 h at 550 °C and cooled to the target temperature in the same feed. The gas mixture was then switched from the reactor to the bypass, and 200 ppm of NOx was added to the mixture. Upon stabilization, the gas mixture was switched back from bypass to the reactor for storage testing for 10 min. The sample was then heated to 600 °C at a rate of 10 °C/min to record the desorption profiles of gases in the effluent.

To further disprove the possibility of formation of Pd(IV) species upon calcination in oxygen, we performed the following experiment. We heated ~ 300 mg of 1 wt% Pd/SSZ-13 in dry oxygen in the quartz reactor [the reactor has valves that allow to isolate it from ambient atmosphere upon installation/removal] at 600 °C for 3 hours, cooled it down to room temperature in dry air flow, purged the reactor with dry nitrogen. Then we moved the reactor to the moisture and oxygen-free glove box without exposure to ambient air, collected the pink powder of Pd/SSZ-13 from the reactor in a 20 ml vial with a screw-cap with a septum. We took a gas-phase sample (1ml) from that vial with a GC syringe, injected it in the GC and analyzed the gas phase to confirm absence of oxygen.

Then through the septum, we introduced a minimum amount of pure de-aerated H_2O. The sample turned yellow, characteristic of Pd(II) hydrated ions. If during the interaction with water the reduction of Pd(IV) to Pd(II) were indeed to take place, then the following red-ox reaction would occur: Pd(IV) + 2 e → Pd(II). If Pd accepts two electrons, water has to give electrons which can only occur via: $H_2O - 2e \rightarrow 2H^+ + 1/2O_2$. If Pd(IV) were indeed reduced to Pd(II), it would produce 14 micromoles of O_2 during this red-ox process. In the ~20 ml vial, this amount of oxygen would be equivalent to ~0.3% of oxygen by volume. This amount (and even much smaller oxygen amount) would be easily detectable with a GC. We injected 1 ml of the gas-phase from the closed vial with a GC syringe and observed no oxygen in the gas phase. Thus, no oxygen was produced, and no Pd(IV) was formed during Pd/SSZ-13 heating in oxygen.

XAS spectra were collected at X-ray beamline 9-1 of the Argonne National Laboratory. The storage ring electron energy was 7 GeV and the ring current was in the range of 495-500 mA. Prior to these measurements, each powder sample was loaded into a cell. The XAS data were collected in the fluorescence mode. Samples were scanned at energies near the Pd *K* absorption edge (24,350 eV). Standards (PdO, Pd foil and $K_2[PdCl_6]$ were scanned as well. PdO and $K_2[PdCl_6]$ were mixed with BN prior to scanning). 1 wt% Pd/SSZ-13 sample in Fig. S1 was calcined in air in the XAS cell at 350 °C for 1 hour, then cooled down in the air flow and XANES recorded at room temperature.

X-ray Photoelectron Spectroscopy (XPS) experiments were performed using a Physical Electronics Quantera scanning X-ray microprobe. This system uses a focused monochromatic Al Kα X-ray (1486.7 eV) source for excitation and a spherical section analyzer. The instrument has a 32 element multichannel detection system. The 80 W X-ray beam focused to 100 μm diameter was rastered over a 1.1 × 0.1 mm rectangle on the sample. The X-ray beam was incident normal to the sample and the photoelectron detector was at 45° off-normal. High-energy-resolution spectra were collected using a pass-energy of 69.0 eV with a step size of 0.125 eV. Note that the samples experienced variable degrees of charging. Low-energy electrons at ~1 eV, 20 μA and low-energy Ar^+ ions were used to minimize this charging. First, the 0.1 and 1 wt% Pd samples were measured as is. The samples then were heated in 10% O_2/He for 1 h at 600 °C (ramping rate 10 °C/min), followed by cooling down in O_2/He to room temperature in a flow cell attached to the XPS system. The pretreated samples were immediately transferred into the UHV chamber without exposure to the open air for the first XPS analysis. Note that following the heating treatment, adventitious

carbon, ideal for binding energy (BE) calibration, became absent. Therefore, all binding energies were referenced to a Si 2p BE of SSZ-13 of 102.7 eV.

Computational Details and Models

We performed periodic DFT calculations using the PW91 exchange-correlation functional with dispersion correction (PW91-D2).[1,2] Vienna *ab initio* simulation package (VASP) [3,4] was employed for these calculations. Ultrasoft pseudopotentials [5,6] were used as implemented in the VASP package. The large size of the unit cell (see below) allowed us to sample the Brillouin zone using the Γ point only [7]. A plane-wave basis was used with a cutoff energy of 400 eV.

The monoclinic unit cell of the CHA framework consists of 36 T atoms. It was optimized for the pure silicate structure with dimensions: a = b = 13.675 Å, c = 14.767 Å; $\alpha = \beta = 90^o$, $\gamma = 120^o$ [8]. Two Si atoms in the unit cell located in one six-member ring were replaced with Al. The negative charges around the Al sites were compensated by the M^{2+} ion or M^+ (M = Pd or Pt) and H^+ cations or their complexes. All atoms were allowed to relax until the force on each atom was less than 5×10^{-2} eV/Å during the geometry optimization.

The total binding energy BE of all neutral ligands (CO, NO, H_2O, and C_2H_4) is calculated as follows:

$$BE = E[ZEO/M(L1)_n(L2)_m] - E[ZEO/M] - n\times E(L1) - m\times E(L2)$$

where $ZEO/M(L1)_n(L2)_m$ (n = 1, 2 or 3) is the energy of the optimized zeolite system together with the metal (M = Pd or Pt) cation and the adsorbed molecule(s); E[ZEO/M] are the energies of the pristine zeolite system, where the framework negative charges are compansated by various cationic species considered, while E(L1) and E(L2) are the energies of the adsorbate molecule(s) in the gas phase.

The adsorption energies of certain ligand (L1 or L2) in the M (M = Pd or Pt) complexes $M(L1)_n(L2)_m$, (n=1-3, m = 0 - 2) located in the pores of CHA zeolite are calculated as follows:

$$BE_{L1} = E[ZEO/M(L1)_n(L2)_m] - E[ZEO/M(L1)_{n-1}(L2)_m] - E(L1)$$

$$BE_{L2} = E[ZEO/M(L1)_n(L2)_m] - E[ZEO/M(L1)_n(L2)_{m-1}] - E(L2)$$

in the cases where there are two types of adsorbed ligands, L_1 and L_2 corresponds to the order of the ligands in the notation of the structure. For example in $Pd^{2+}(CO)(C_2H_4)$ structure CO is first ligand (L_1) and C_2H_4 is the second one (L_2).

Consistent with these definitions, negative values of BE imply a favorable interaction.

The vibrational frequencies were calculated using a normal mode analysis where the elements of the Hessian were approximated as finite differences of gradients, displacing each atomic center by 1.5×10^{-2} Å either way along each Cartesian direction. All calculated C-O vibrational frequencies were shifted by the difference of the calculated harmonic frequency of the free CO obtained with the same computational approach and the experimentally measured (anharmonic) frequency of CO in the gas phase (i.e., 2143 cm^{-1}):

$$H(C\text{-}O)^{calc} = H_{calculated} - H_{calculated}(CO\text{-}gas) + 2143.$$

In this case, the calculated ν_{CO} frequencies are corrected for both the anharmonicity (which is 35 cm^{-1} for gas phase CO) and the systematic error of the computational method, as reported earlier [9]. Such correction cannot be applied for the N-O vibrational frequencies due to the change in the oxidation state, when NO ligands are adsorbed to the metal species.

References

[1]. J.P. Perdew, Y. Wang. Accurate and Simple Analytic Representation of the Electron-Gas Correlation Energy. *Phys. Rev. B* **1992**, *45*, 13244–13249.

[2]. S. Grimme. J. Comput. Chem. 2006, 27, 1787−1799.

[3]. G. Kresse, J. Hafner. Ab Initio Molecular-Dynamics Simulation of the Liquid-Metal-Amorphous-Semiconductor Transition in Germanium. *Phys. Rev. B* **1994**, *49*, 14251–14269.

[4]. G. Kresse, J. Furthmüller. Efficiency of Ab-Initio Total Energy Calculations for Metals and Semiconductors Using a Plane-Wave Basis Set. *Comput. Mater. Sci.* **1996**, *6*, 15–50.

[5]. D. Vanderbilt. Soft Self-Consistent Pseudopotentials in a Generalized Eigenvalue Formalism. *Phys. Rev. B* **1990**, *41,* 7892–7895.

[6]. G. Kresse, J. Hafner. Norm-Conserving and Ultrasoft Pseudopotentials for First-Row and Transition-Elements. *J. Phys.*: *Condens. Matter* **1994**, *6,* 8245–8257.

[7]. Y. Jeanvoine, J. Angyan, G. Kresse, J. Hafner. Bronsted Acid Sites in HSAPO-34 and Chabazite: An Ab Initio Structural Study. *J. Phys. Chem. B* **1998**, *102,* 5573–5580.

[8]. Ch. Baerlocher, L.B. McCusker. Database of Zeolite Structures. http://www.iza-structure.org/databases/.

[9]. K. Khivantsev, N. R. Jaegers, L. Kovarik, J. C. Hanson, F. F. Tao, Y. Tang, X. Zhang, I. Z. Koleva, H. A. Aleksandrov, G. N. Vayssilov, Y. Wang, F. Gao, J. Szanyi, Achieving Atomic Dispersion of Highly Loaded Transition Metals in Small-pore Zeolite SSZ-13: a New Class of

High-capacity and High-efficiency Low Temperature CO and Passive NOx Adsorbers, Angew. Chem. Int. Ed., 2018, doi:10.1002/anie.201809343.

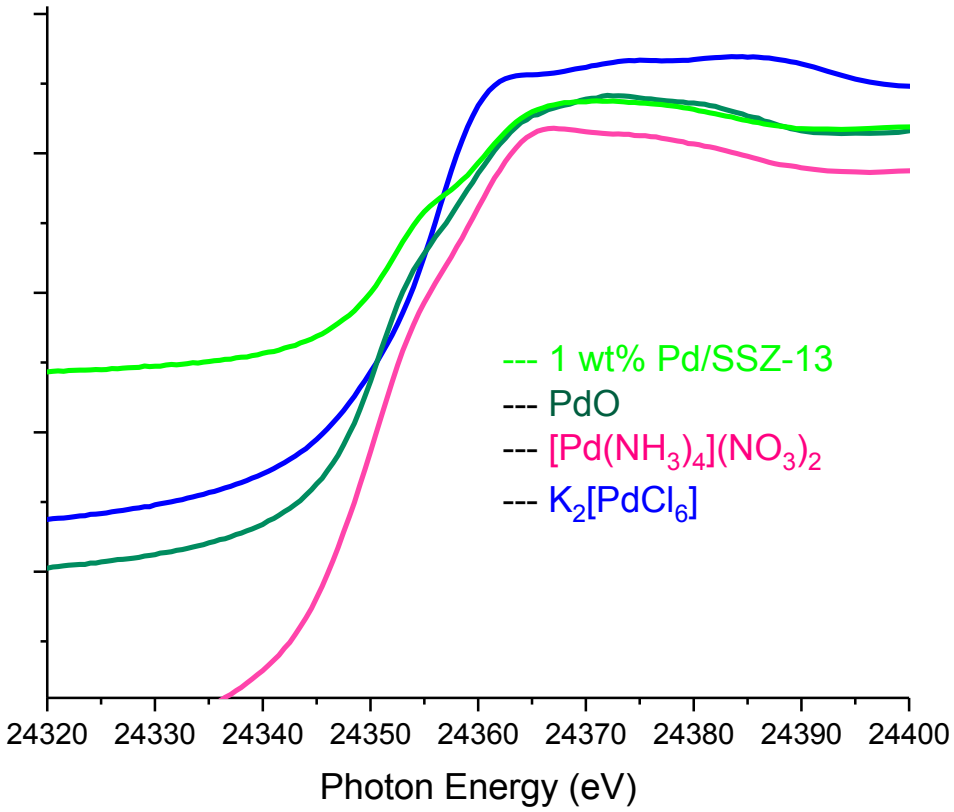

Figure S1. XANES region at the Pd K-edge of standards PdO, $[Pd(NH_3)_4](NO_3)_2$, $K_2[PdCl_6]$ and comparison with air calcined 1 wt% Pd/SSZ-13.

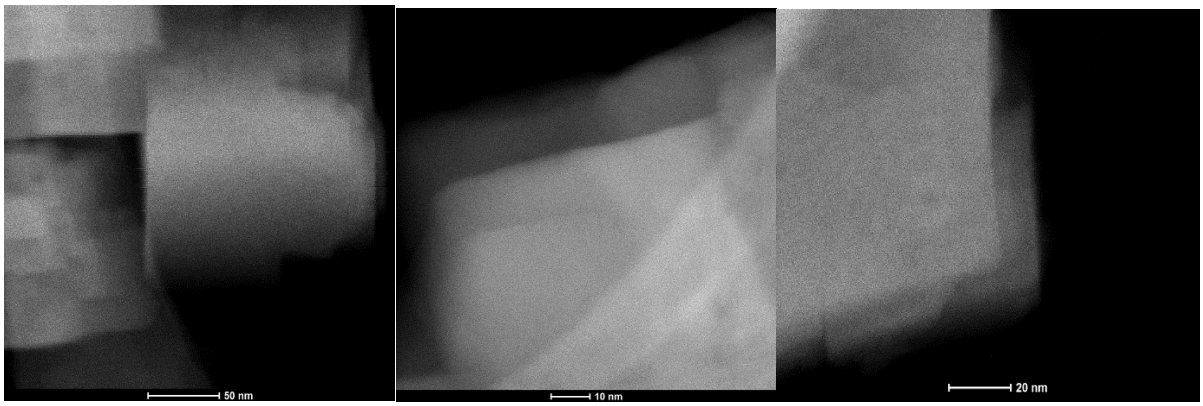

Figure S2. Cryo-HAADF-STEM images of of 1 wt% Pd/SSZ13 with Si/Al ratio 6 showing very high dispersion of Pd (no agglomeration).

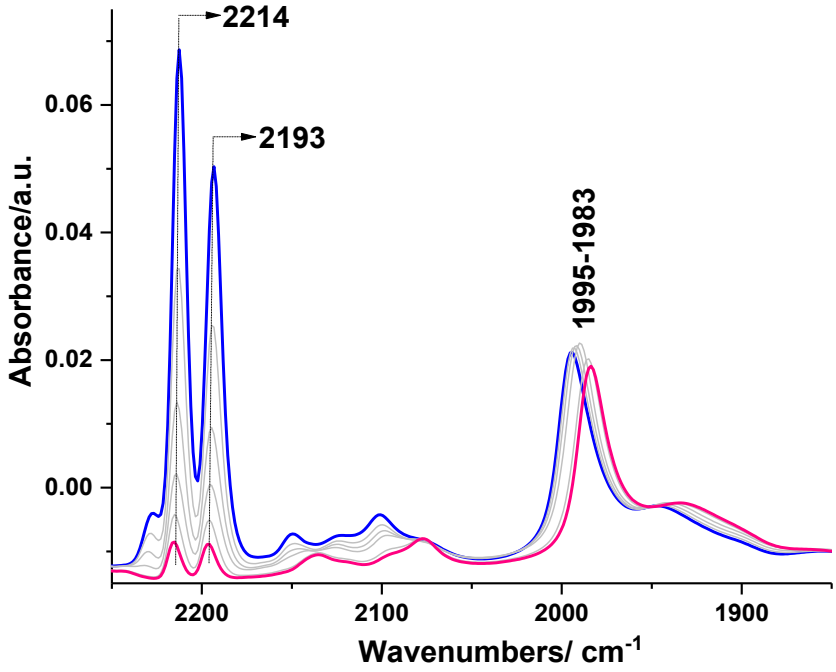

Figure S3. FTIR spectra under vacuum (from 5 Torr CO adsorbed to 0.001 Torr) on 1 wt% Pd/SSZ-13 with Si/Al=6 pre-reduced in the presence of CO (10 Torr) at 400 °C for 1 hr in the infra-red cell.

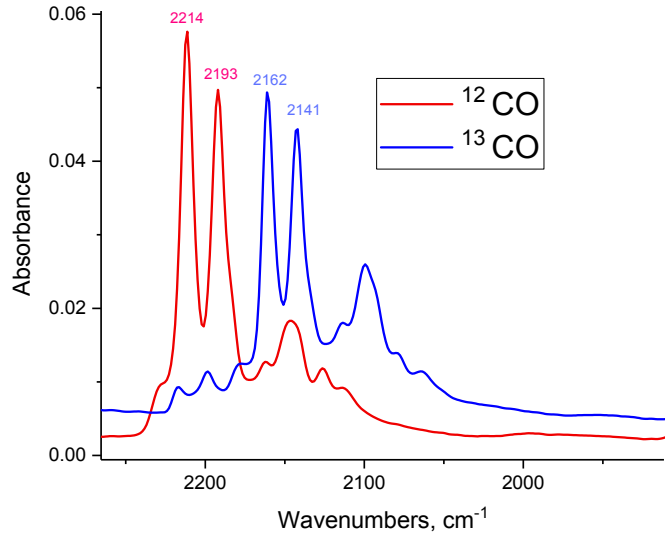

Figure S4. FTIR spectra during 5 Torr ^{13}CO adsorption on 1 wt% Pd/SSZ-13 with Si/Al=6 exposed to 5 Torr ^{12}CO prior to that.

Figure S5. Visual changes to 1 wt% Pd/SSZ-13 with Si/Al ratio 6 single-atom material: a). in the presence of moisture b). dehydrated under helium or oxygen (note that these changes are reversible; when the pink sample is stored in the glove box in the absence of moisture it retains its colour; as soon as water is added in the glovebox or the sample is taken out of the glovebox, the colour changes to yellowish) c). Pd/SSZ-13 exposed to CO d). $Pd(II)(CO)_2$/SSZ-13 exposed to a single pulse of ethylene with the formation of classical colourless (in the VIS region) $Pd(II)(CO)(C_2H_4)$ complex.

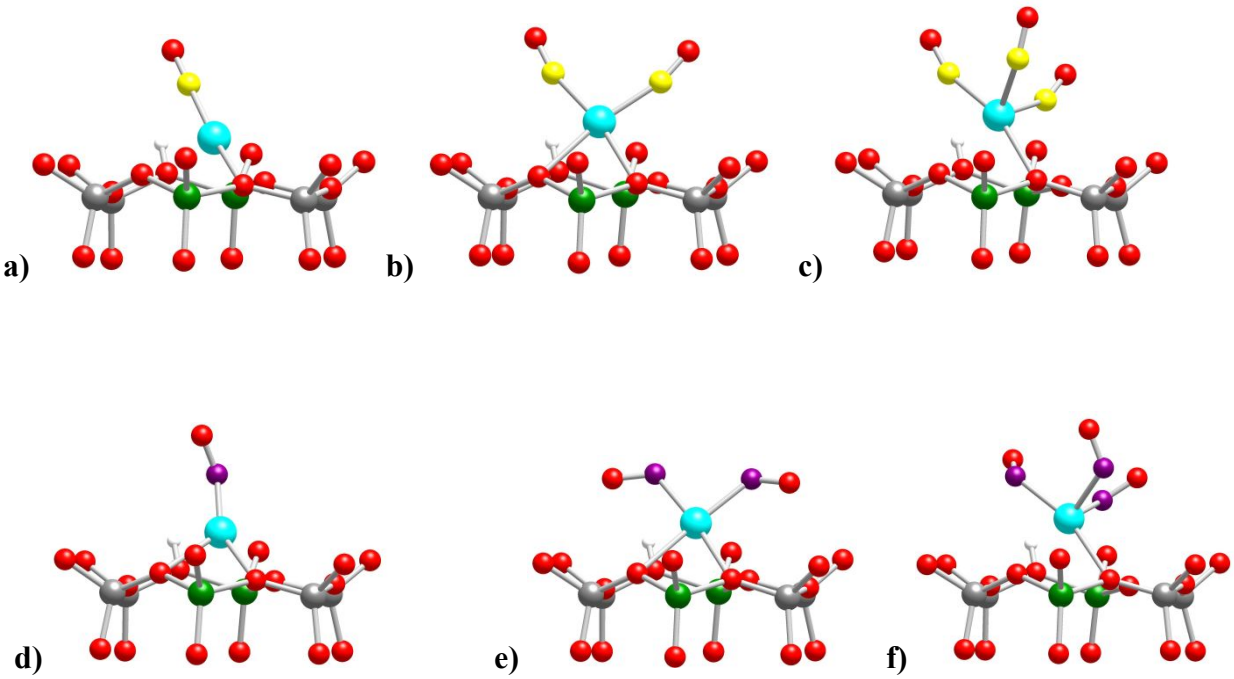

Figure S6. Optimized structures of selected Pd^+ complexes located in a six-membered ring of CHA: (a) $Pd^+(CO)$; b) $Pd^+(CO)_2$, c) $Pt^+(CO)_3$, d) $Pd^+(NO)$, e) $Pd^+(NO)_2$ and f) $Pd^+(NO)_3$. For visual clarity only local structure around the complex is shown and in some cases different views of the complexes are presented. Color coding: Si – gray; O – red; Al – green; H – white; C – yellow; N – purple; Pd – cyan.

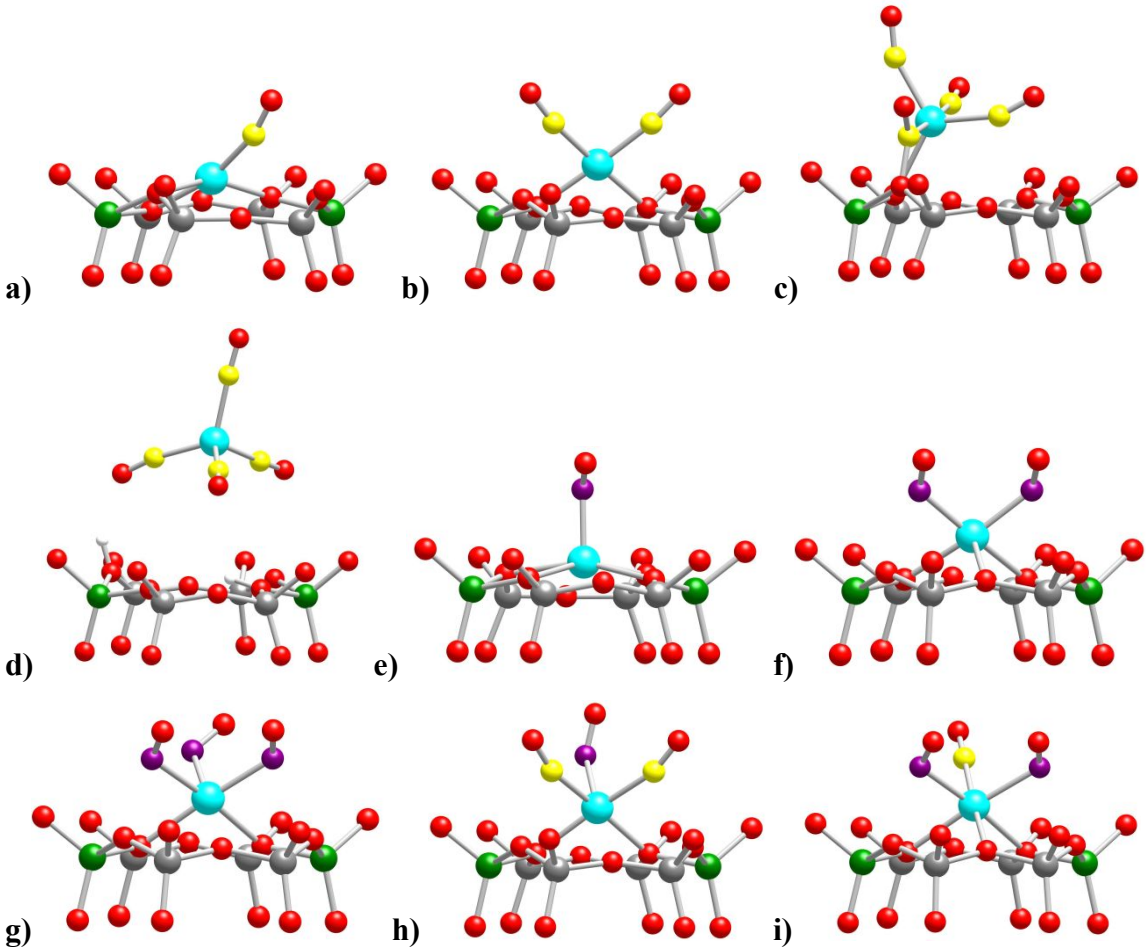

Figure S7. Optimized structures of selected Pd^{2+} complexes located in a six-membered ring of CHA: (a) $Pd^{2+}(CO)$; b) $Pd^{2+}(CO)_2$, c) $Pd^{2+}(CO)_4$ zeo, d) desorbed $Pd^{0}(CO)_4$ unit; e) $Pd^{2+}(NO)$, f) $Pd^{2+}(NO)_2$ and g) $Pd^{2+}(NO)_3$; mixed complexes: h) $Pd^{2+}(CO)_2(NO)$, i) $Pd^{2+}(CO)(NO)_2$. For visual clarity only local structure around the complex is shown and in some cases different views of the complexes are presented. Color coding: Si – gray; O – red; Al – green; H – white; C – yellow; N – purple; Pd – cyan.

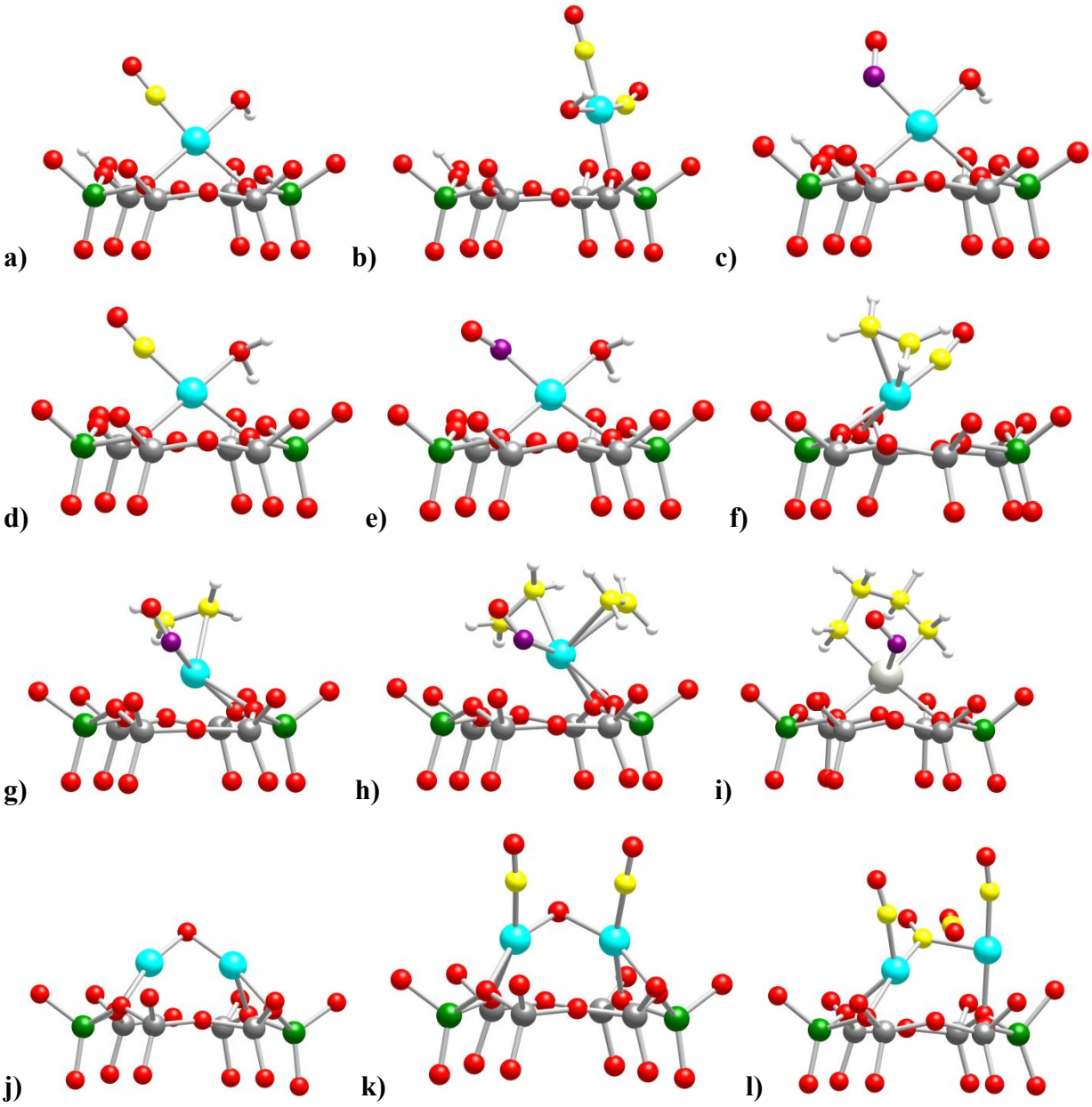

Figure S8. Optimized structures of selected Pd^{2+} complexes located in a six-membered ring of CHA: a) $Pd^{2+}(CO)(OH)$, b) $Pd^{2+}(CO)_2(OH)$, c) $Pd^{2+}(NO)(OH)$, d) $Pd^{2+}(CO)(H_2O)$, e) $Pd^{2+}(NO)(H_2O)$, f) $Pd^{2+}(CO)(C_2H_4)$, g) $Pd^{2+}(NO)(C_2H_4)$, h) $Pd^{2+}(NO)(C_2H_4)_2$ and i) $Pd^{2+}(NO)(C_4H_8)$. Models with $Pd^{2+}(O)Pd^{2+}$ dimer: j) pristine dimer, k) $Pd^{2+}(CO)(O)Pd^{2+}(CO)$, l) $Pd^{2+}(CO)_2(O)Pd^{2+}(CO)_2$ (one CO_2 is desorbed). Color coding: Si – gray; O – red; Al – green; H – white; C – yellow; N – purple; Pd – cyan.

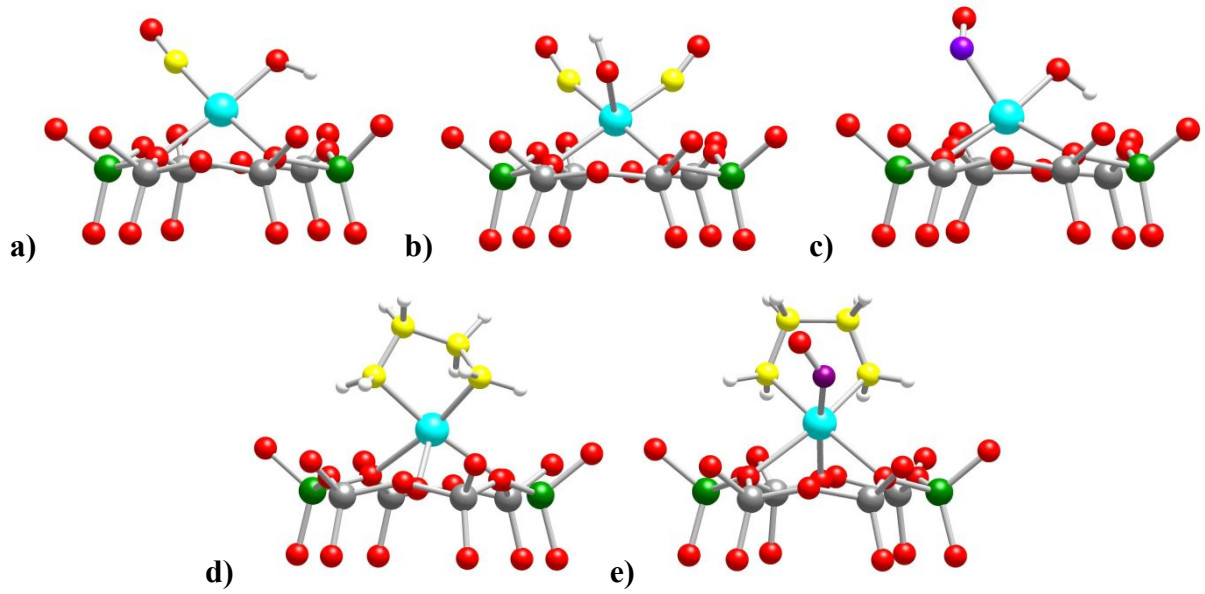

Figure S9. Optimized structures of selected Pd^{3+} and Pd^{4+} complexes located in a six-membered ring of CHA: a) $Pd^{3+}(CO)(OH)$, b) $Pd^{3+}(CO)_2(OH)$, c) $Pd^{3+}(NO)(OH)$, d) $Pd^{4+}(C_4H_8)(O)$ and e) $Pd^{4+}(NO)(C_4H_8)(O)$. Color coding: Si – gray; O – red; Al – green; H – white; C – yellow; N – purple; Pd – cyan.

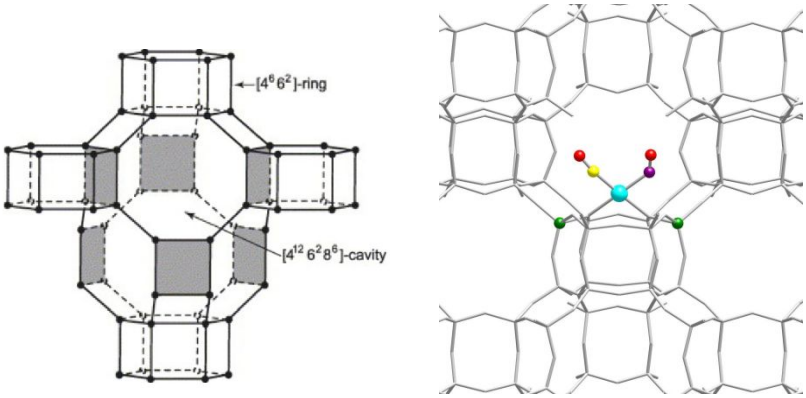

Figure S10. Crystallographic structure of SSZ-13 (chabazite) material. The diameter of the cavity is ~0.85 nm.

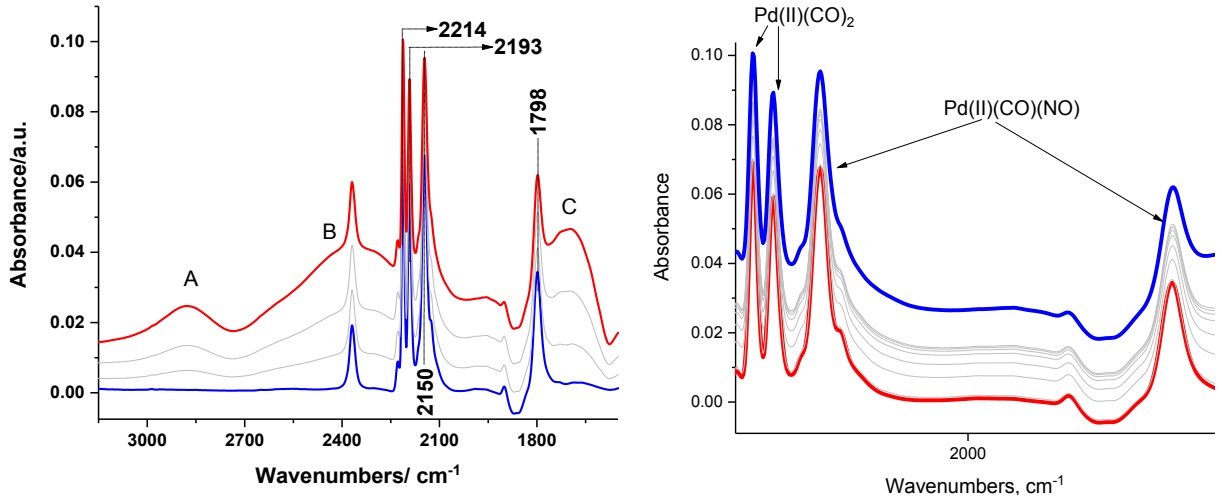

Figure S11. FTIR of sequential 6 Torr H_2O adsorption on $Pd(II)(CO)_2$ and Pd(NO)(CO) in SSZ-13 (1 wt% Pd, Si/Al=6). Both complexes are stable in the presence of water (6 Torr added). ABC structure is the typical triplet feature developed upon water adsorption on zeolites in IR spectra (see, for example, Nature of "A,B,C"-type infrared spectra of strongly hydrogen-bonded systems; pseudo-maxima in vibrational spectra Claydon, M. F.; Sheppard, N., Journal of the Chemical Society [Section] D: Chemical Communications (1969).

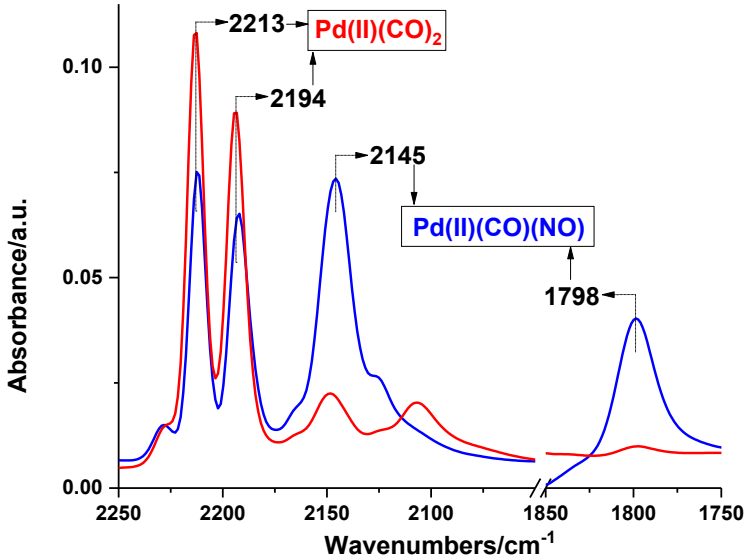

Figure S12. NO adsorption (0.2 Torr) on $Pd(CO)_2$/SSZ-13 with Si/Al=6.

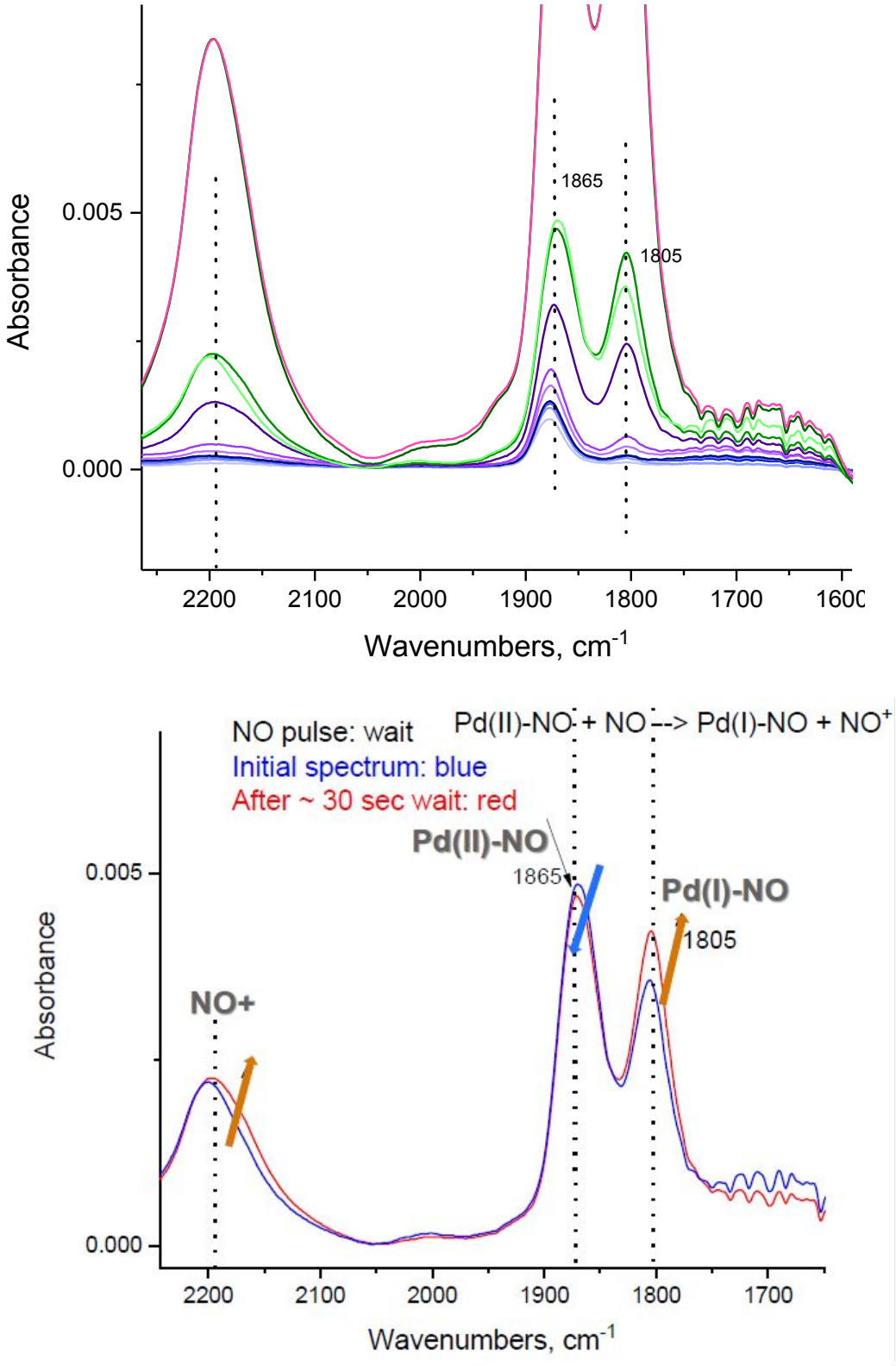

Figure S13. A) Upper figure: NO adsorption on 1 wt% Pd/SSZ-13 with Si/Al=6. B). More detailed look at NO adsorption on Pd/SSZ-13 with Si/Al=6: more specifically, after a single NO

pulse the spectrum is immediately taken after pressure stabilization, and then the next spectrum is taken 30 seconds after the NO pulse. We provide the first direct experimental evidence of Pd(II) reduction by NO. NO is a free radical and addition of its unpaired electron to Pd(II) can reduce Pd(II) to Pd(I): this is exactly what we observe while looking at NO stretching frequencies; more specifically, the band pf Pd(II)-NO goes down at the expense of Pd(I)-NO that gets formed. We have previously assigned the 1,805 cm^{-1} to Pd(I)-NO on the basis of DFT calculations and common sense. Now, however, we have been able to capture this transformation in detail. The reduction of Pd(II) to Pd(I) also frees up 1 Al-O site and form nitrosyl (or alternatively nitrosonium) ion NO^+ which occupies the newly available cationic position (the IR signature of this NO+ in proximity to the reduced Pd center is at about ~2,170 cm^{-1}) :

$Pd(II) + NO \rightarrow Pd(I)\text{-}NO + NO^+$

This finding is the first direct extension and confirmation of our previous findings for Cu(II)/SSZ-13 system during its interaction with NO that we have reported earlier: Kwak, J. H., Lee, J. H., Burton, S. D., Lipton, A. S., Peden, C. H. and Szanyi, J. (2013), A Common Intermediate for N_2 Formation in Enzymes and Zeolites: Side-On Cu–Nitrosyl Complexes. Angew. Chem. Int. Ed., 52: 9985-9989. doi:10.1002/anie.201303498

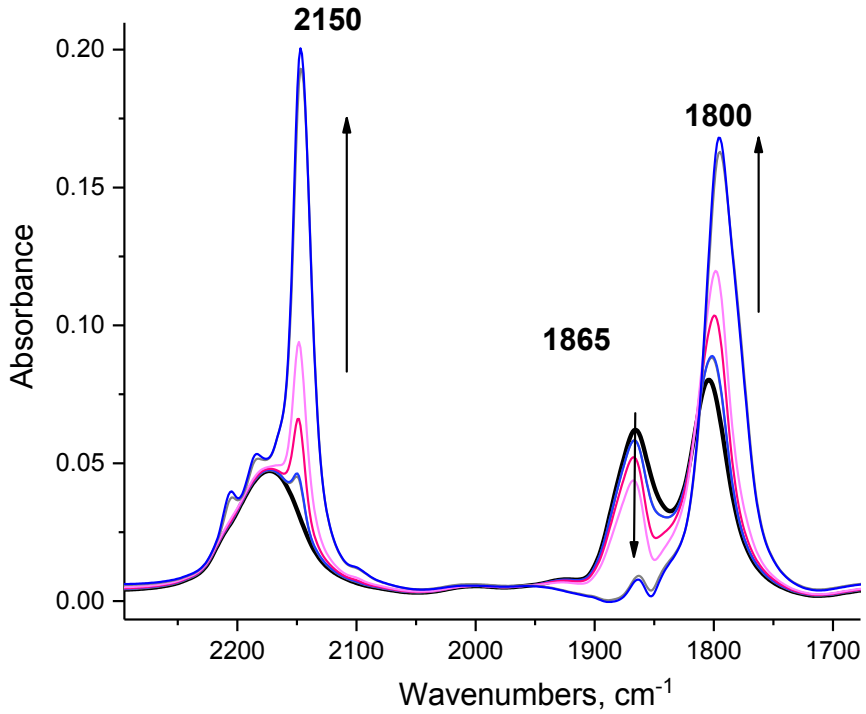

Figure S14. FTIR spectra collected during step-wise addition of 0.5 Torr CO adsorption on an NO saturated 1wt% Pd/H-SSZ-13 sample.

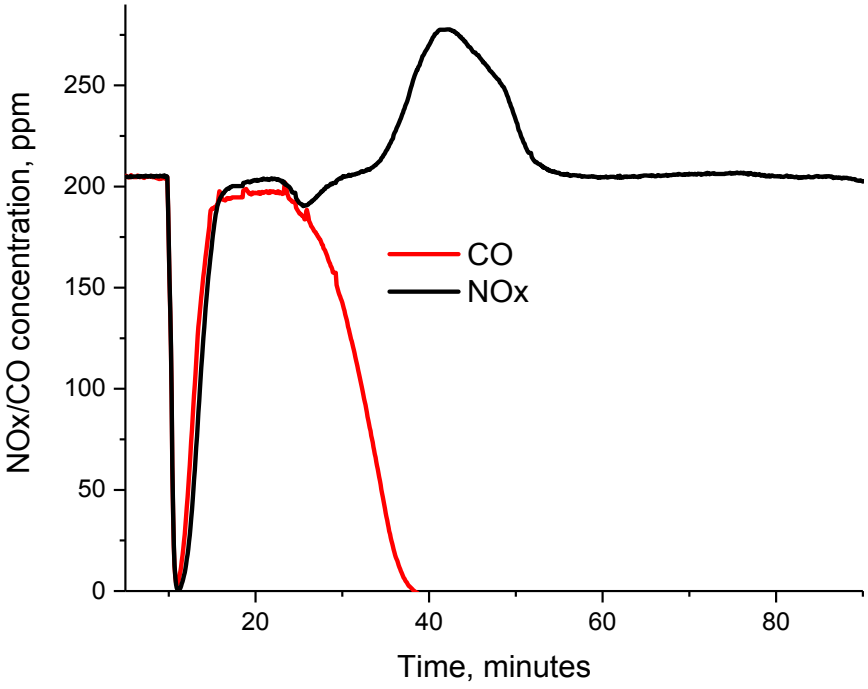

Figure S15. NOx and CO abatement performance of 1 wt% Pd SSZ-13 with Si/Al = 6. NOx adsorption at 100 °C for 10 min (after 10 min bypass) followed with TPD (10 °C/min). The feed gas mixture contains 200 ppm of NOx, 14% O_2, 3 % H_2O with with 200 ppm CO.

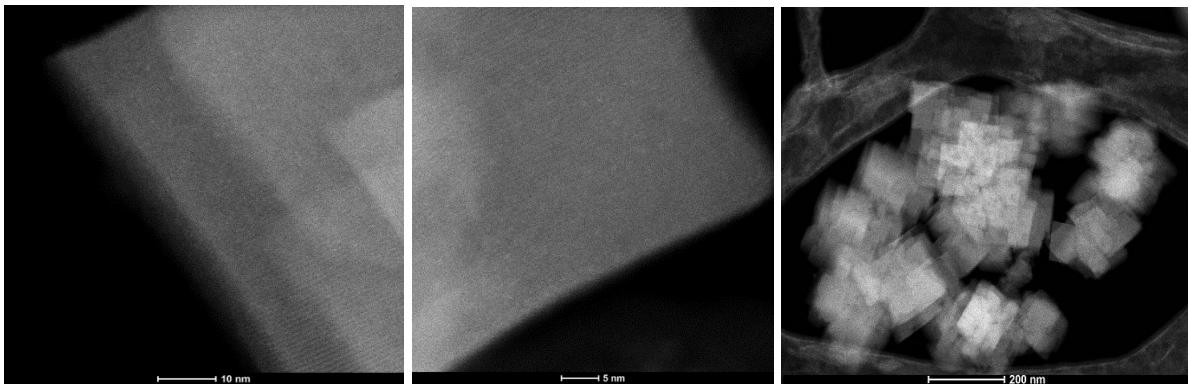

Figure S16. HAADF-STEM images of 1 wt% Pt/SSZ13 with Si/Al ratio 6.

Table S1. Binding energies of the neutral ligands (in kJ/mol), vibrational frequencies of diatomic ligands (υ(L) in cm^{-1}), elongation of the bond length(s) in the ligands with respect to isolated molecule in gas phase, Pd-ligand and Pd-O_{zeo} distances (Δd(A-B), d(Pd-L), d(Pd-O_{zeo}), respectively, in pm), and number of the unpaired electrons in the systems, N_s.

Structures	BE	BE_{L1}	BE_{L2}	υ(L)[a]	Δd(A-B)[b]	d(Pd-L)	d(Pd-O_{zeo})	N_s
Pd^{+}							220;222;225	1
$Pd^{3+}H_{zeo}$	85[c]					149	215;217;224;227	1
$Pd^{+}(NO)$	-226			1804	0.3	181	220;231	0
$Pd^{+}(NO)_2$	-306	-80		1816;1739	0.1;0.8	197;223	223;235	1
$Pd^{+}(NO)_3$	-403	-97		1817;1740;1717	0.0;0.3;0.9	201;203;206	236;242	0
$Pd^{+}(CO)$	-158			2075	1.1	188	214;246;258	1
$Pd^{+}(CO)_2$	-252	-94		2103;2063	0.5;0.7	195;197	224;235	1
$Pd^{+}(CO)_3$	-273	-20		2098;2058;2055	0.6;0.7;0.7	196;201;213	230;248	1
Pd^{2+}							206;206;214;214	0
$Pd^{2+}(CO)$	-87			2114	0.4	188	206;213;214	0
$Pd^{2+}(CO)_2$	-215	-128		2172;2138	-0.2;-0.2	192;192	210;210	0
$Pd^{2+}(CO)_3$					one CO ligand desorbs			
$Pd^{2+}(CO)_{4zeo}$	-271			2178;2133;2122;1845	-0.6;-0.1;0.0;4.4[d]	203;204;206;206	234	0
$Pd^{0}(CO)_{4\ desorbed}$				2119;2073;2068;2012	0.6;0.6;0.7;1.5	199;201;202;202		
$Pd^{2+}(NO)$	-122			1843	-1.1	193	218;219;232;233	1
$Pd^{2+}(NO)_2$	-243	-121		1879;1823	0.1;0.8	197;201	223;235	0
$Pd^{2+}(NO)_3$	-348	-104		1868;1817;1797	-1.1;-1.1;-0.8	205;207;213	229;231;254	1
$Pd^{2+}(CO)(NO)$	-200	-78	-113	2146/1830	-0.1/-1.1	193/199	213;217	1
$Pd^{2+}(CO)_2(NO)$	-252	-130	-37	2132;2111/1822	0.0;0.0/-1.0	198;198/232	219;220	1
$Pd^{2+}(CO)(NO)_2$	-319	-50	-232	2148/1852;1808	-0.3/-1.2;-1.1	199/215;215	232;238;238	0
$Pd^{2+}(CO)(OH)$[e]		-187		2121	0.4/-0.1[g]	187/198	213;219	0
$Pd^{2+}(CO)_2(OH)$		-262		2165;2125	-0.1;0.0/-0.7[g]	189;197/198	215	0
$Pd^{2+}(NO)(OH)$ [f]		-177		1796	-0.1/0.1 [g]	189;198	219;225	1
$Pd^{2+}(H_2O)$[h]	-50				0.5;7.2	206	203;215;217	0
$Pd^{2+}(CO)(H_2O)$[i]	-209	-159	-122	2148	-0.1/0.7;8.0	188/209	209;210	0
$Pd^{2+}(NO)(H_2O)$[j]	-203	-153	-80	1828	-1.1/0.7;6.2	191/214	212;215	1
$Pd^{2+}(C_2H_4)$	-58				4.7	229;229	221;221;234;235	0
$Pd^{2+}(C_4H_8)$	-162[k]							
$Pd^{2+}(CO)(C_2H_4)$	-209	-151	-98	2140	0.1/6.3	188/223;224	206;221	0
$Pd^{2+}(NO)(C_2H_4)$	-201	-144	-79	1807	-0.7/5.8	192/224;224	216;235;254	1
$Pd^{2+}(NO)(C_2H_4)_2$	-258		-136	1817	-1.0/3.4;3.9	203/231;237;243;250	237;237	1
$Pd^{2+}(NO)(C_4H_8)$	-301[k]		-139	1822	-1	200/214;218	227;232;251	1
$Pd^{3+}(CO)(OH)$		-117		2158	-0.3	192/195	210;211	1
$Pd^{3+}(CO)_2(OH)$		-160		2141;2114	0.0;0.1	194;194/217	213;213	1
$Pd^{3+}(NO)(OH)$		-149		1897	-2.3	203/195	212;224	0
$Pd^{4+}(CO)_2(O)$				Spontaneous formation and desorption of CO_2				0
$Pd^{4+}(C_4H_8)(O)$	-141[k]					211;213	225;226;227	0
$Pd^{4+}(NO)(C_4H_8)(O)$	-254[k]	-113		1836	-0.8	199	237;237	3
$Pd^{2+}(O)Pd^{2+}$							214;219/214;219	0
$Pd^{2+}(CO)(O)Pd^{2+}(CO)$	-321			2132/2116	0.3/0.3	188/188	214;219/214;219	0
$Pd^{2+}(CO)_2(O)Pd^{2+}(CO)_2$				Spontaneous formation and desorption of CO_2				

[a] shifted by +35 cm^{-1} since the calculated CO in gas phase 2108 cm^{-1} is lower by 35 cm^{-1} with respect to the experimental value, 2143 cm^{-1}'; the calculated frequencies of NO are not shifted. Part of the data have been reported as Supporting information in ref. [9] and here they are reported for comparison with the new data.
[b] elongation with respect to the isolated ligand
[c] relative energy with respect to Pd^{+} structure
[d] elongation of the bound CO molecule to one O from the zeolite
[g] elongation of OH with respect to Pd^{2+}(OH)/zeo complex
Hydrogen bond between the H from OH and O from the zeolite: [e] 204 pm; [f] 203 pm.
Hydrogen bond between the H from H_2O and O from the zeolite: [h] 147.8 pm; [i] 149.0 pm; [j] 154.5 pm.
[k] With respect to two molecules ethylene

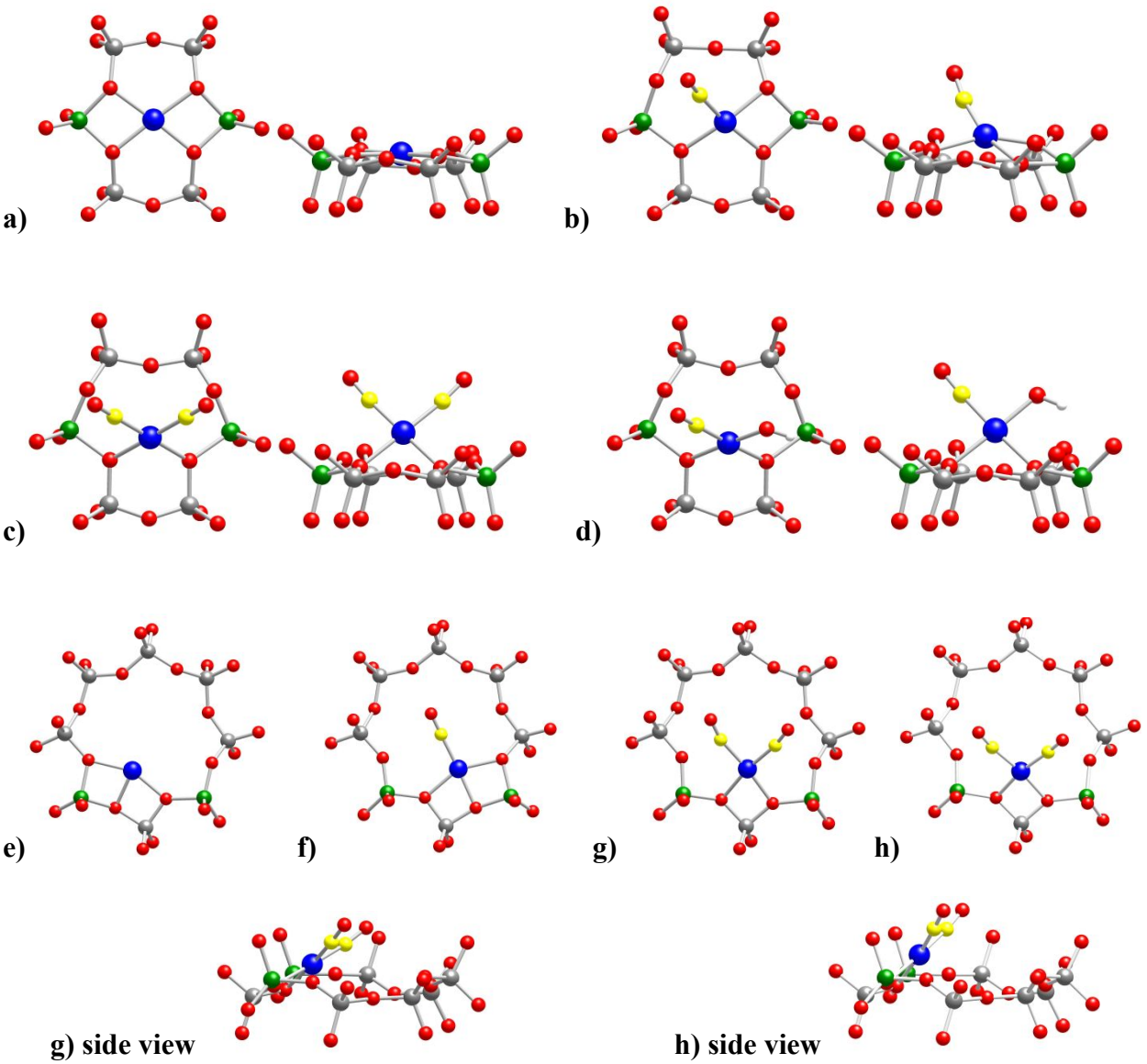

Figure S17. Optimized structures of selected Pt^{2+} complexes located in a six-membered ring of CHA: (a) Pt^{2+}; b) $Pt^{2+}(CO)$; c) $Pt^{2+}(CO)_2$ and d) $Pt^{2+}(CO)(OH)$, as well as located in eight membered ring of CHA: e) Pt^{2+}; f) $Pt^{2+}(CO)$_a; g) $Pt^{2+}(CO)_2$_a; h) $Pt^{2+}(CO)_2$_b. For visual clarity only local structure around the complex is shown and in some cases different views of the complexes are presented. Color coding: Si – gray; O – red; Al – green; H – white; C – yellow; Pt – blue.

Table S2. Binding energies of all the neutral ligands (BE, in kJ/mol) and of the second adsorbed ligand (BE_{L2}, in kJ/mol), vibrational frequencies of diatomic (C-O) ligands (x(L) in cm^{-1}), elongation of the C-O bond length(s) in the ligands with respect to the isolated CO molecule in gas phase, Pt-ligand distances (in pm) (Pt-L), distances between Pt cation and zeolite O centers ($Pt\text{-}O_{zeo}$) and number of the unpaired electrons in the systems, N_s.

Str.	BE	BE_{L2}	x(L)[a]	Δd(A-B)[b]	d(Pt-L)	$d(Pt\text{-}O_{zeo})$	N_s
Pt^{2+}						206;206;212;212	0
$Pt^{2+}(CO)$	-134		2108	0.8	185	208;211;211	0
$Pt^{2+}(CO)_2$	-318	-184	2182;2136	-0.1;0.0	189;189	209;209	0
$Pt^{2+}(OH)$					190	202;210;211	1
$Pt^{2+}(CO)(OH)$	-181		2146	0.1	188;194	209;209	1
Pt^{2+} 8 mem. ring						200;206;211	0
$Pt^{2+}(CO)$_a 8 mem. ring	-309		2138	0.5	186	202;211;212	0
$Pt^{2+}(CO)$_b 8 mem. ring	-309		2134	0.4	186	202;211;213	0
$Pt^{2+}(CO)_2$_a 8 mem. ring	-481	-173	2156;2108	0.2;0.5	190;190	206;210	0
$Pt^{2+}(CO)_2$_b 8 mem. ring	-479	-170	2179;2135	0.0;0.1	189;190	205;210	0

[a] the frequencies are shifted by +35 cm^{-1} since the calculated C-O vibrational frequency for a CO molecule in gas phase 2108 cm^{-1} is lower by 35 cm^{-1} with respect to the experimental value, 2143 cm^{-1}.

[b] elongation with respect to the isolated ligand in gas phase

Table S3. XPS data acquisition parameters.

XPS wide scan data acquisition parameters:							
No	Transition	Start (eV)	End (eV)	Inc (eV)	Time/DataPt (s)	Pass Energy (eV)	
1	Su1s	1350.00	0.00	-0.50	0.287	140.00	
XPS narrow (high energy resolution) scan data files:							
No	Transition	Start (eV)	End (eV)	Inc (eV)	Time/DataPt (s)	Pass Energy (eV)	
6	O1s	541.00	523.00	-0.13	0.862	69.00	
5	C1s	294.00	276.00	-0.13	1.293	69.00	
4	Pd3d	354.00	328.00	-0.13	6.467	69.00	
3	N1s	408.00	390.00	-0.20	2.874	112.00	
2	Al2p	83.00	65.00	-0.13	0.862	69.00	
1	Si2p	111.00	93.00	-0.13	0.862	69.00	

Table S4. Calculated weight % of each element for 1 and 0.1 wt% Pd/SSZ-13 with Si/Al=6 "as is" and after various treatments.

Weight % Table (Calculated from XPS data)

Area	Comment	C1s	O1s	Al2p	Si2p	Pd3d
1wt% Pd/SSZ-13 Si/Al=6	(batch 1) As is	0.87	57.49	4.32	36.80	0.51
1wt% Pd/SSZ-13 Si/Al=6	(batch 1) 600C O2	0.04	56.57	4.90	37.95	0.54
1wt% Pd/SSZ-13 Si/Al=6	(batch 1) 600C O2	0.00	55.92	4.95	38.60	0.52
1wt% Pd/SSZ-13 Si/Al=6	(batch 1) NO RT	0.05	56.27	4.75	38.32	0.61
0.1wt% Pd/SSZ-13 Si/Al=6	As is	0.69	57.79	4.44	36.99	0.09
0.1wt% Pd/SSZ-13 Si/Al=6	600C O2	0.11	56.60	4.84	38.34	0.12
0.1wt% Pd/SSZ-13 Si/Al=6	600C NO RT	0.05	57.31	4.64	37.97	0.04

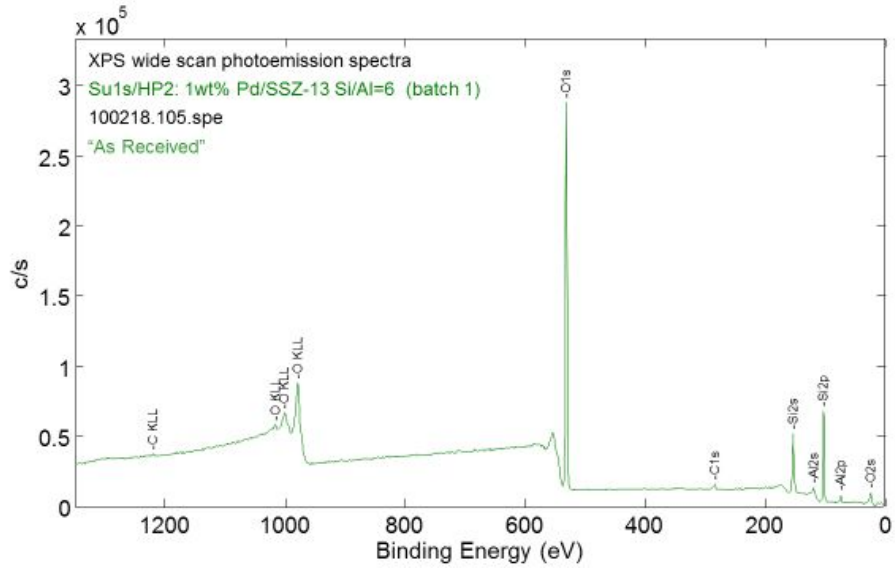

Figure S18. Wide-line XPS scan of 1 wt% Pd/SSZ-13 with Si/Al=6 as is.

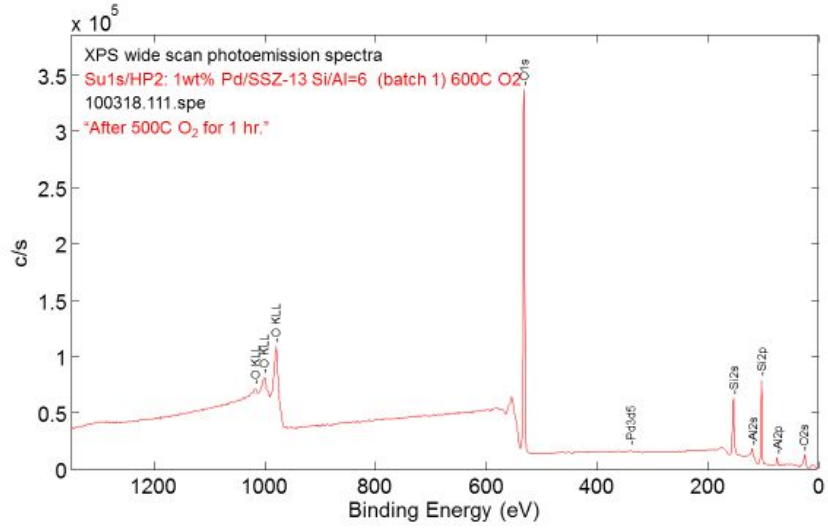

Figure S19. Wide-line XPS scan of 1 wt% Pd/SSZ-13 with Si/Al=6 calcined at 600 ºC (taken at the first sample area).

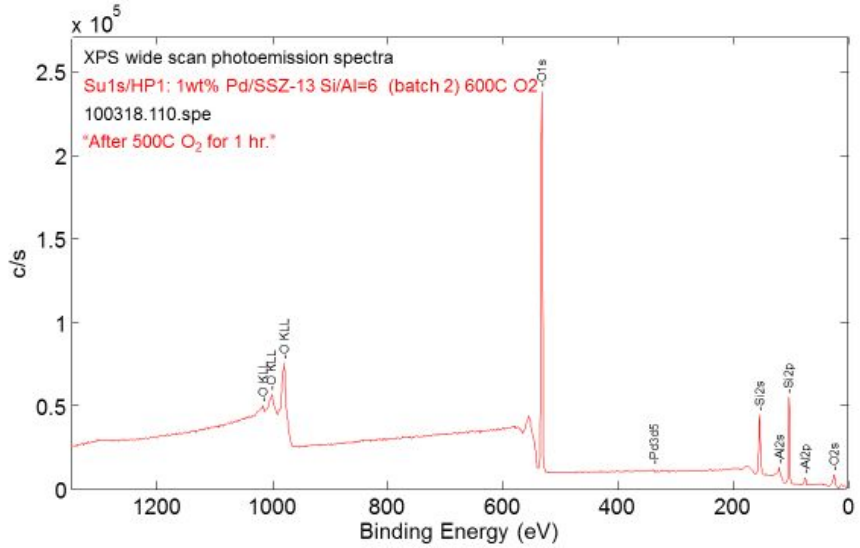

Figure S20. Wide-line XPS scan of 1 wt% Pd/SSZ-13 with Si/Al=6 calcined at 600 ºC (taken at the 2nd sample area, different than the first one).

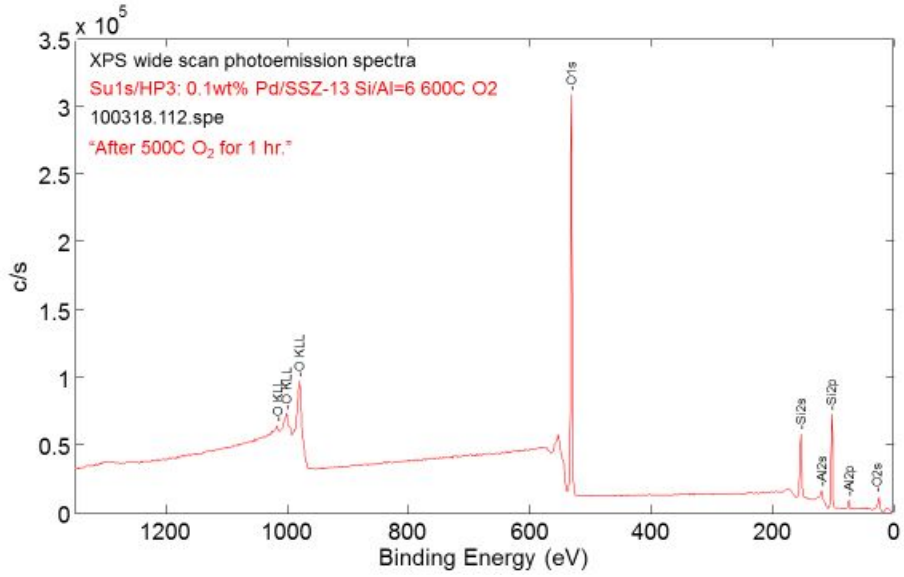

Figure S21. Wide-line XPS scan of 0.1 wt% Pd/SSZ-13 with Si/Al=6 calcined at 600 ºC.

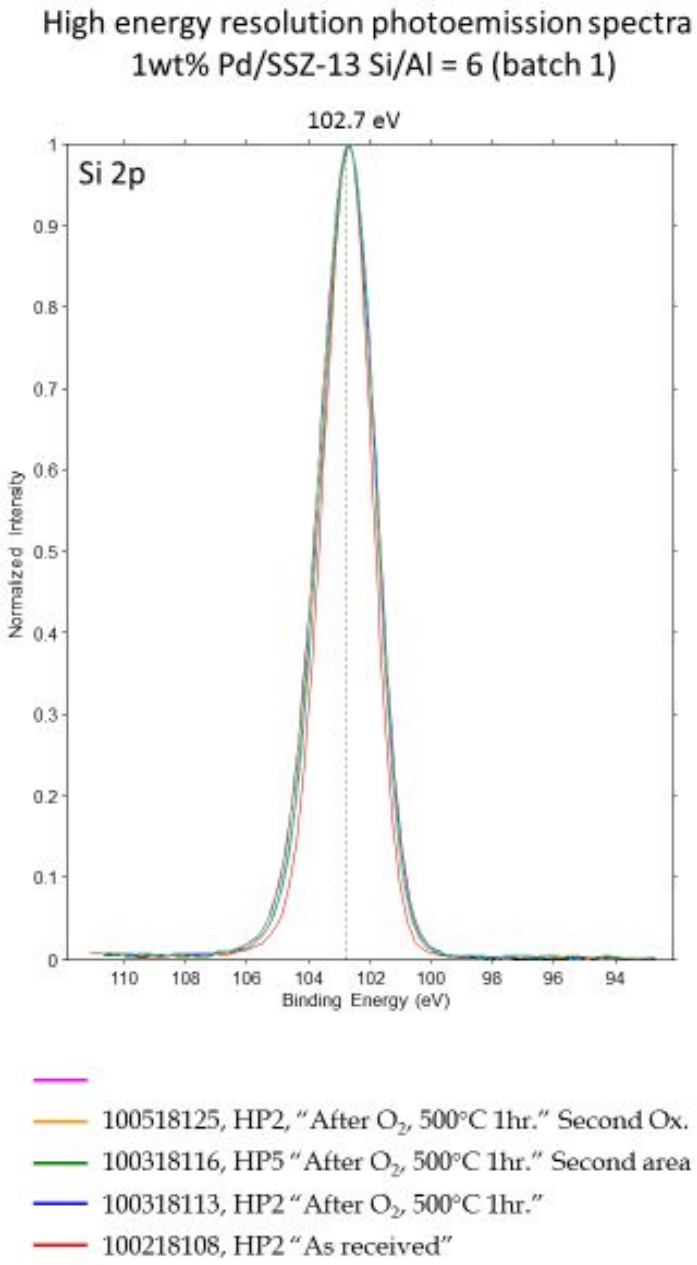

Figure S22. High-resolution XPS scan of Si2p region for 1 wt% Pd/SSZ-13 with Si/Al=6 as is and treated under various conditions (sample was calcined at 600 ºC in oxygen).

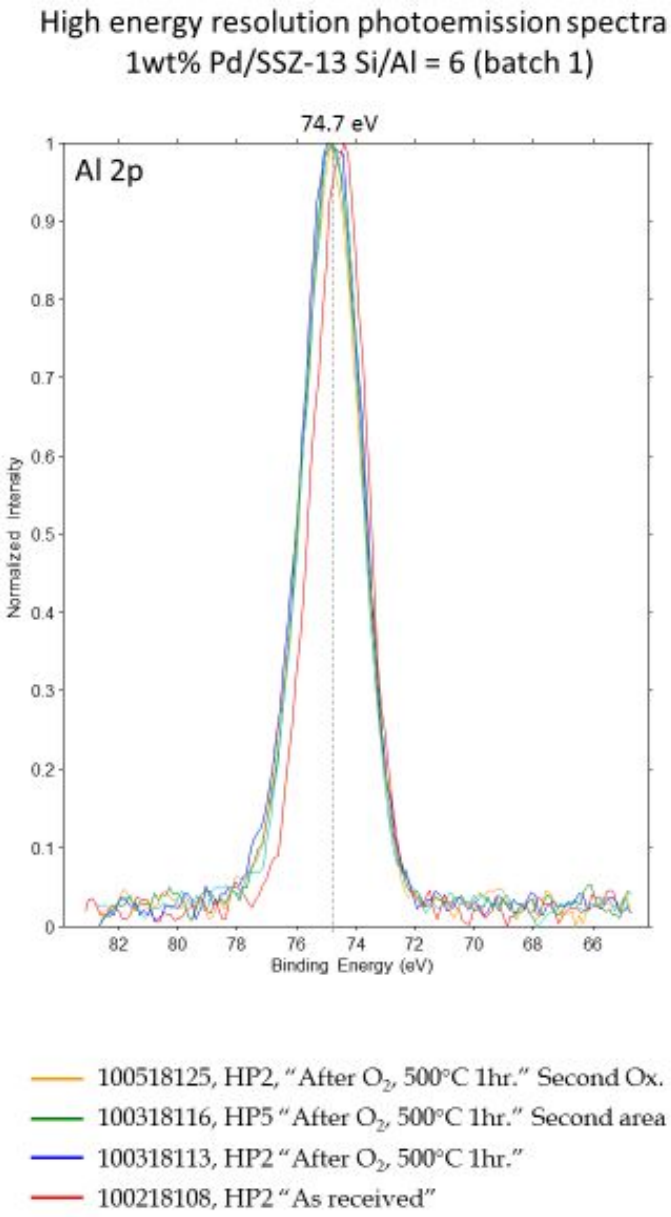

Figure S23. High-resolution XPS scan of Al2p region for 1 wt% Pd/SSZ-13 with Si/Al=6 as is and treated under various conditions (sample was calcined at 600 ºC in oxygen). Importantly, we report for the first time the shift of Al BE to the left (by ~0.4 eV to higher binding energy, meaning that Al site becomes more positive) due to water leaving zeolite micropores: this confirms that water occluded in zeolite micropores under ambient conditions interacts predominantly with Al-O sites (and not O-Si sites, hence no shift in the Si BE during dehydration in Fig. S22)); thus, interaction of Al-O-H (where Al is the framework T site) with water modulates the properties of T-sites to an extent (makes them more basic) which has significant importance for chemical (organics) conversion in zeolites in the presence and absence of water. This finding complements, for example, the following data for water interaction with the zeolite obtained with state-of-the-art solid-state MAS NMR techniques: Genesis and Stability of Hydronium Ions in Zeolite Channels, Meng Wang, Nicholas R. Jaegers, Mal-Soon Lee, Chuan

Wan, Jian Zhi Hu, Hui Shi, Donghai Mei, Sarah D. Burton, Donald M. Camaioni, Oliver Y. Gutiérrez, Vassiliki-Alexandra Glezakou, Roger Rousseau, Yong Wang, Johannes A. Lercher, J. Am. Chem. Soc.2019, 141, 8, 3444-3455.

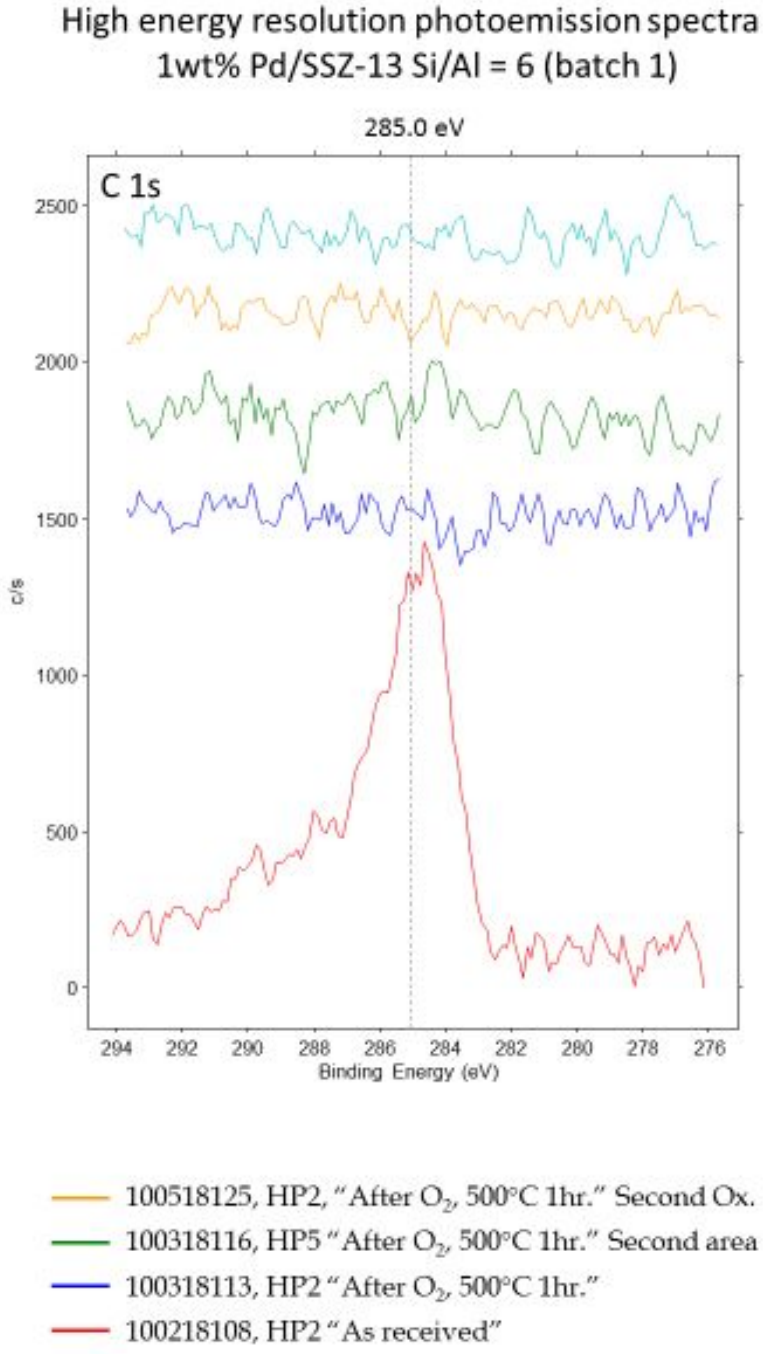

Figure S24. High-resolution XPS scan of C1s region for 1 wt% Pd/SSZ-13 with Si/Al=6 as is and treated under various conditions (sample was calcined at 600 ºC in oxygen).

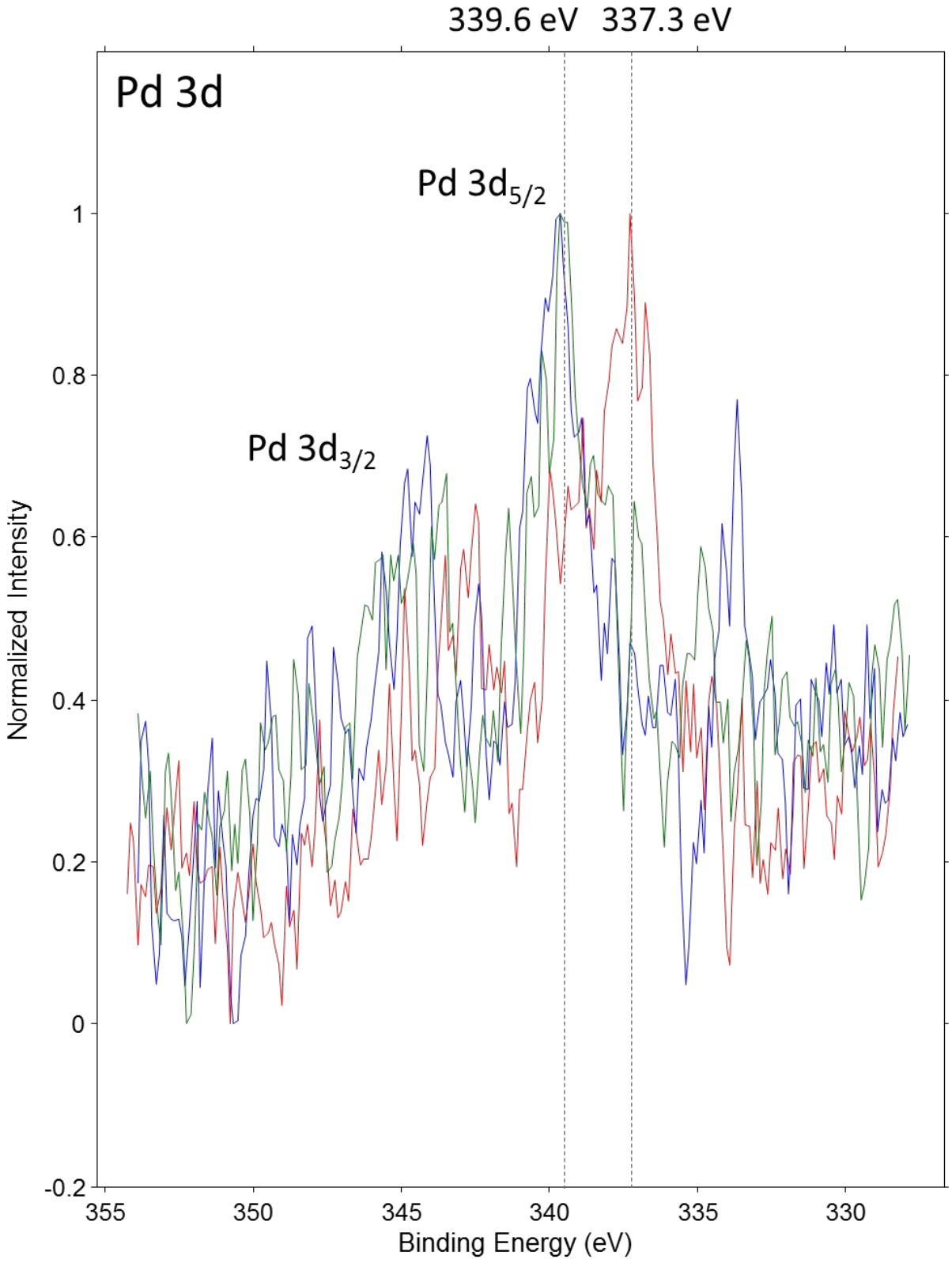

Figure S25. High-resolution XPS spectra for 0.1 wt% Pd/SSZ-13 with Si/Al ratio 6 before (red) and after heating in oxygen at 600ºC (experiments performed quasi *in-situ*).

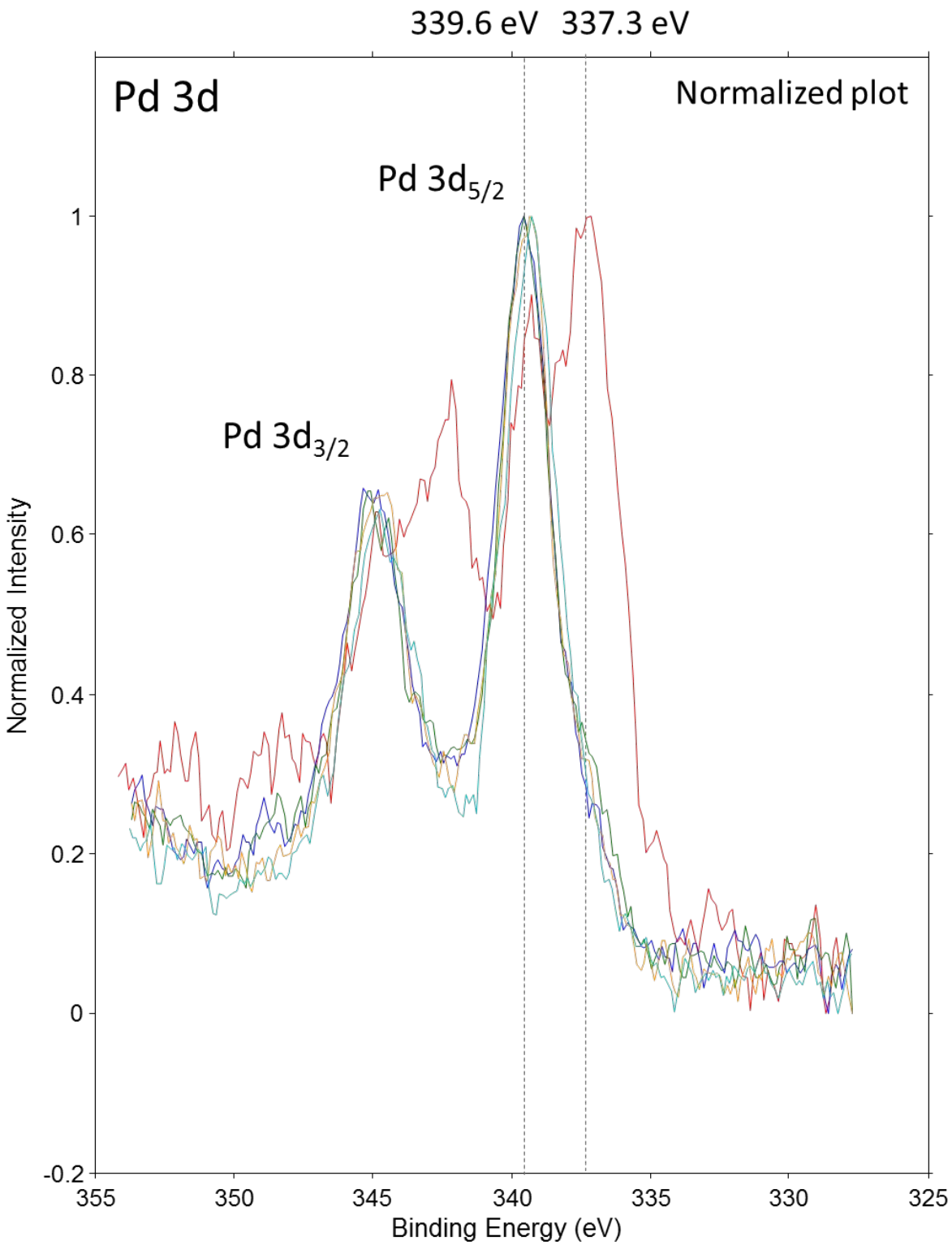

Figure S26. High-resolution XPS spectra for 1 wt% Pd/SSZ-13 with Si/Al ratio 6 before (red) and after heating in oxygen at 600ºC (experiments performed quasi *in-situ*).

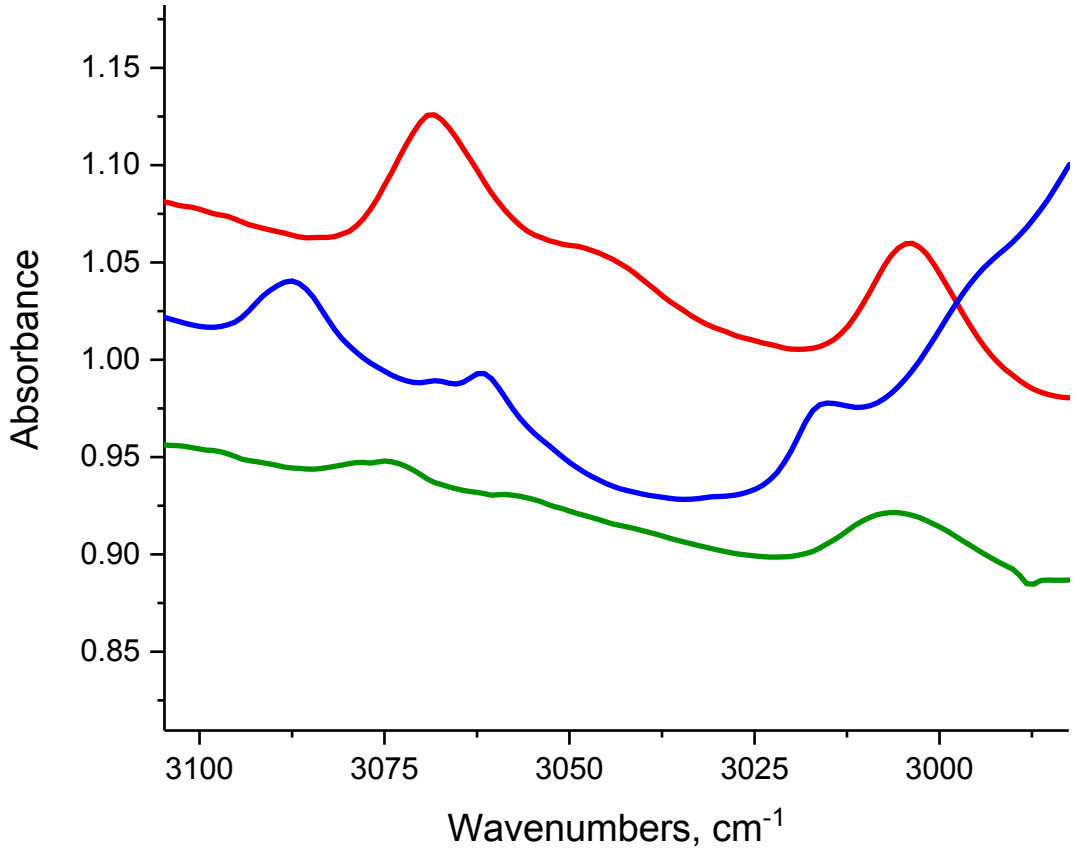

Figure S27. C-H stretching regions of $Rh(C_2H_4)_2$ on zeolite (blue line), alumina (red line) and $Rh(CO)(C_2H_4)(Acac)$ (green line).

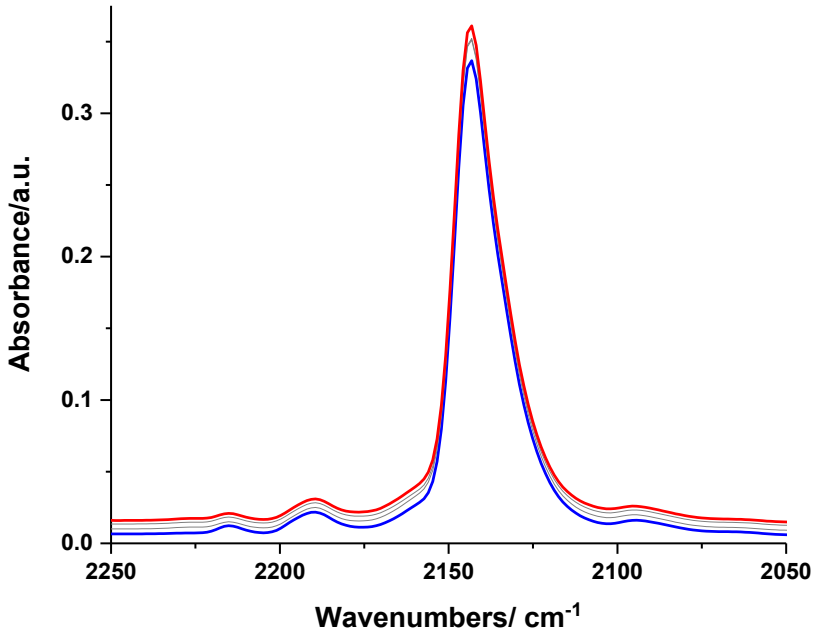

Figure S28. FTIR spectra of the CO adsorption (10 Torr) on the Pd(II)(CO)(C_2H_4)/SSZ-13 with Si/Al ratio 6.

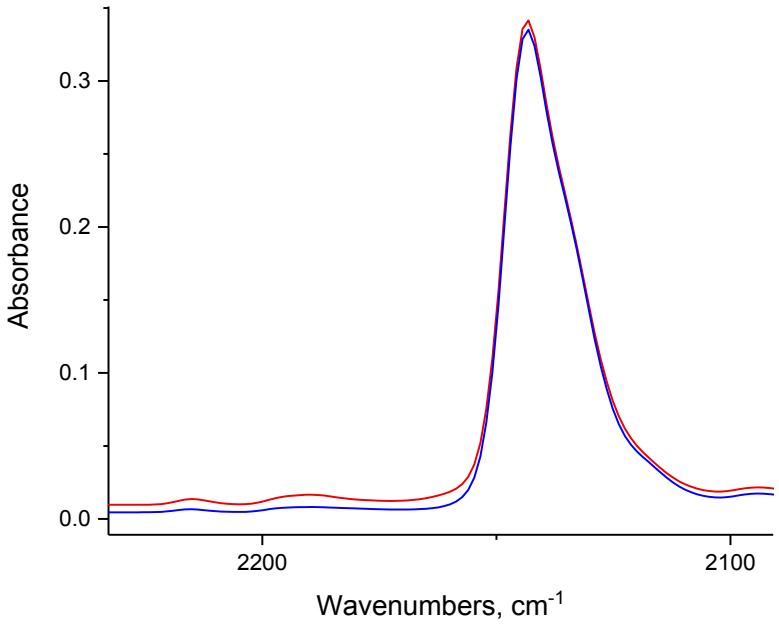

Figure S29. FTIR spectra of the high vacuum (10^{-6}-10^{-7} Torr) on the Pd(II)(CO)(C_2H_4)/SSZ-13 with Si/Al ratio 6.

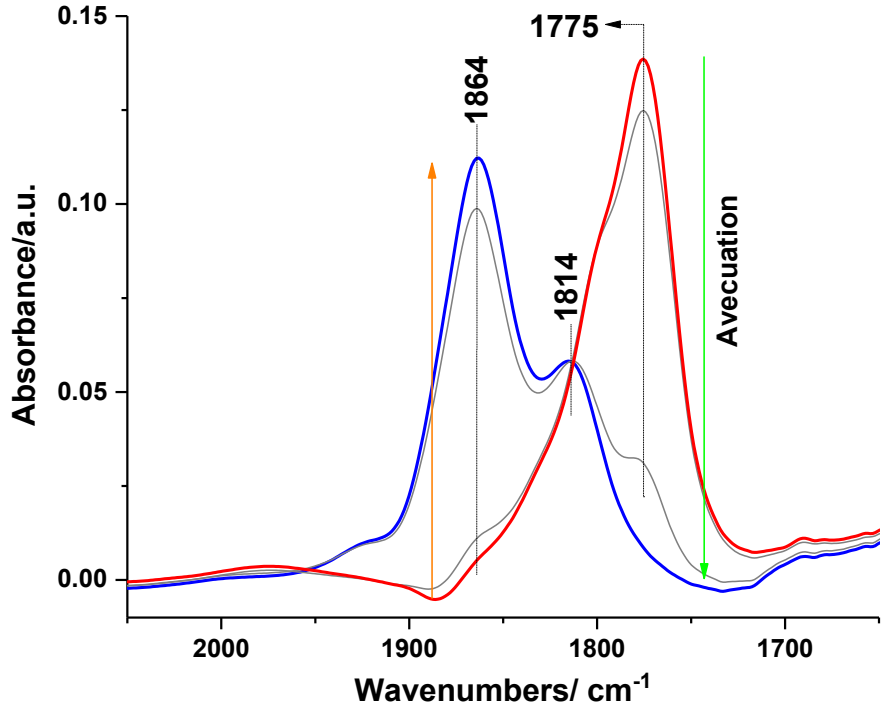

Figure S30. FTIR spectra of applying high vacuum on the Pd(II)(NO)(C_2H_4)/SSZ-13 with Si/Al ratio 6.

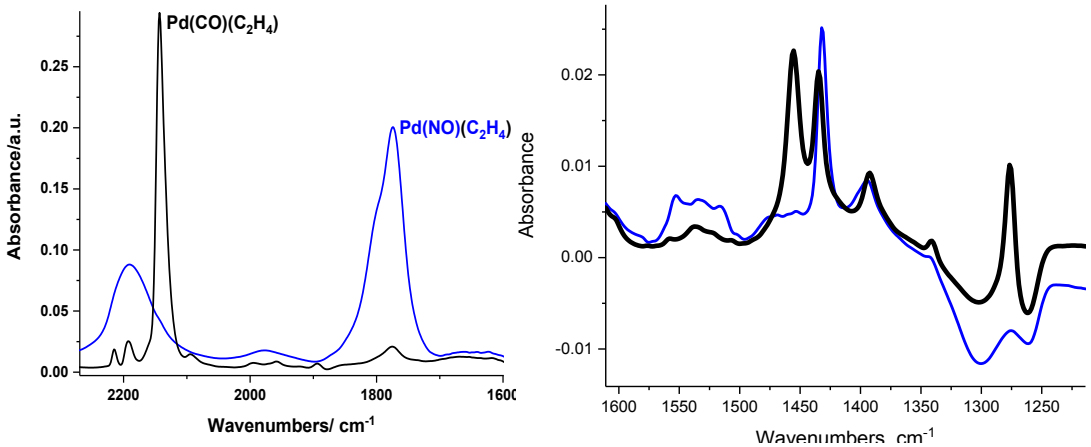

Figure S31. FTIR spectra of the comparison between Pd(II)(CO)(C_2H_4) (black spectrum) and Pd(NO)(C_2H_4)/SSZ-13 (blue spectrum) with Si/Al ratio 6 after C_2H_4 adsorption on Pd carbonyl and nitrosyl complexes: CO/NO stretching and C=C vibrations regions are shown in addition to C-H stretching region in the main text.

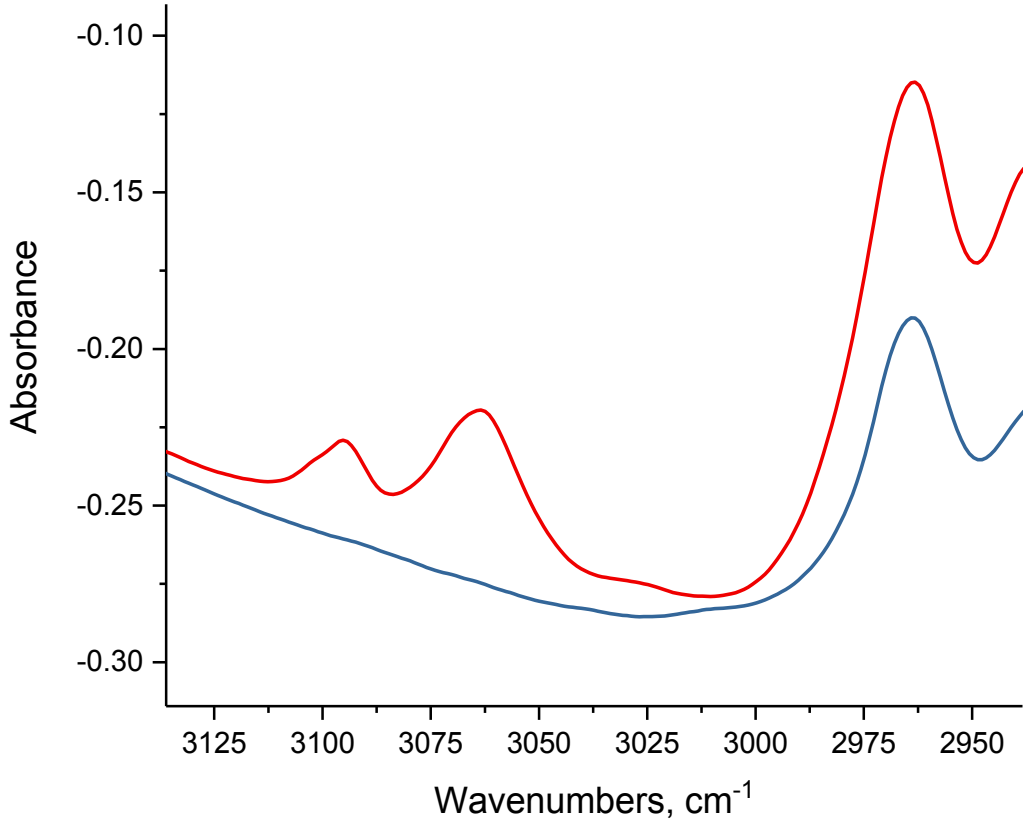

Figure S32. C-H stretching region of 5% butadiene adsorption on zeolite (blue line before adsorption, red line after butadiene-1,3 adsorption).

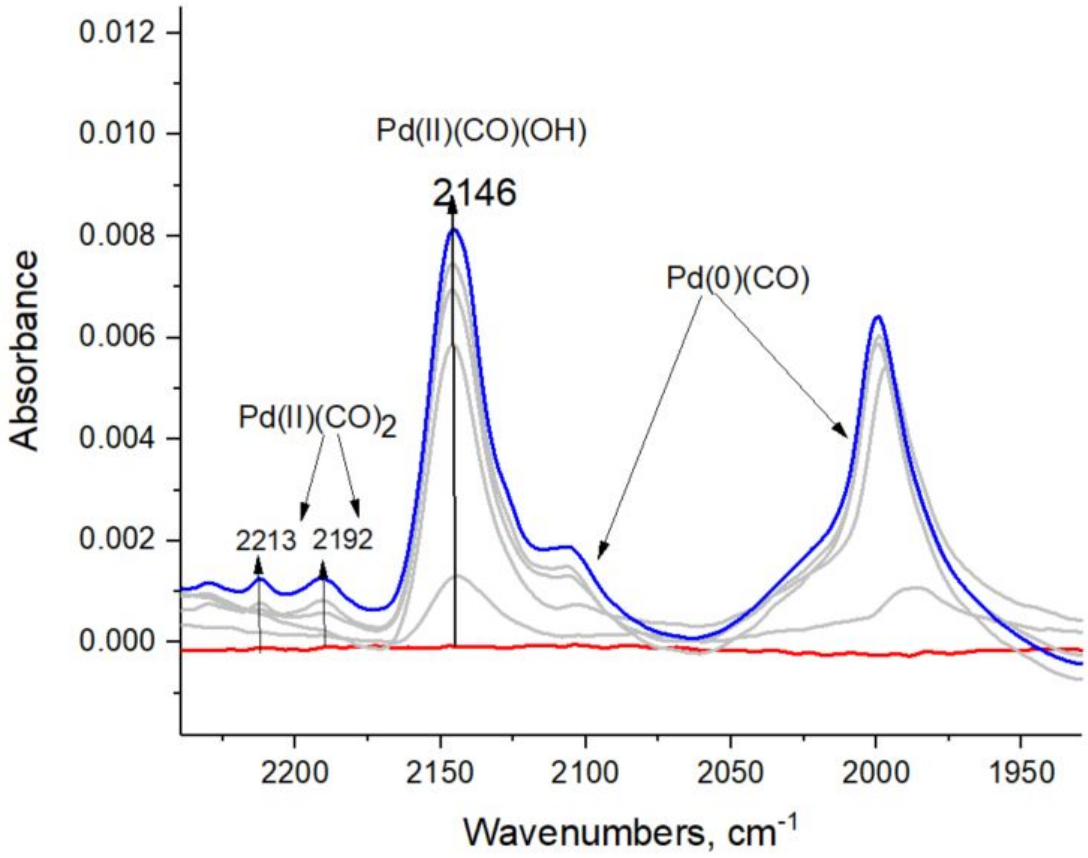

Figure S33. FTIR spectra during 5 Torr CO adsorption on 1 wt% Pd/SSZ-13 with Si/Al=30. Consistent with our previous work, $Pd(II)(CO)_2$ are not stabilized selectively because at this Si/Al ratio with between 1 to 2 Al atoms per unit cell the fraction of paired Al T-sites in the vicinity is small. The major species is Pd(II)(CO)(OH) and a significant fraction of linear CO adsorbed on metal Pd(0) clusters and particles can be seen, consistent with findings in our Angew. Chem. Paper (**ref. 8 main text**) where HADDF-STEM and PNA performance testing show that for 1 wt% Pd/SSZ-13 sample with Si/Al~30 the amount of atomically dispersed Pd is ~30%, the rest is PdO nanoparticles and clusters.

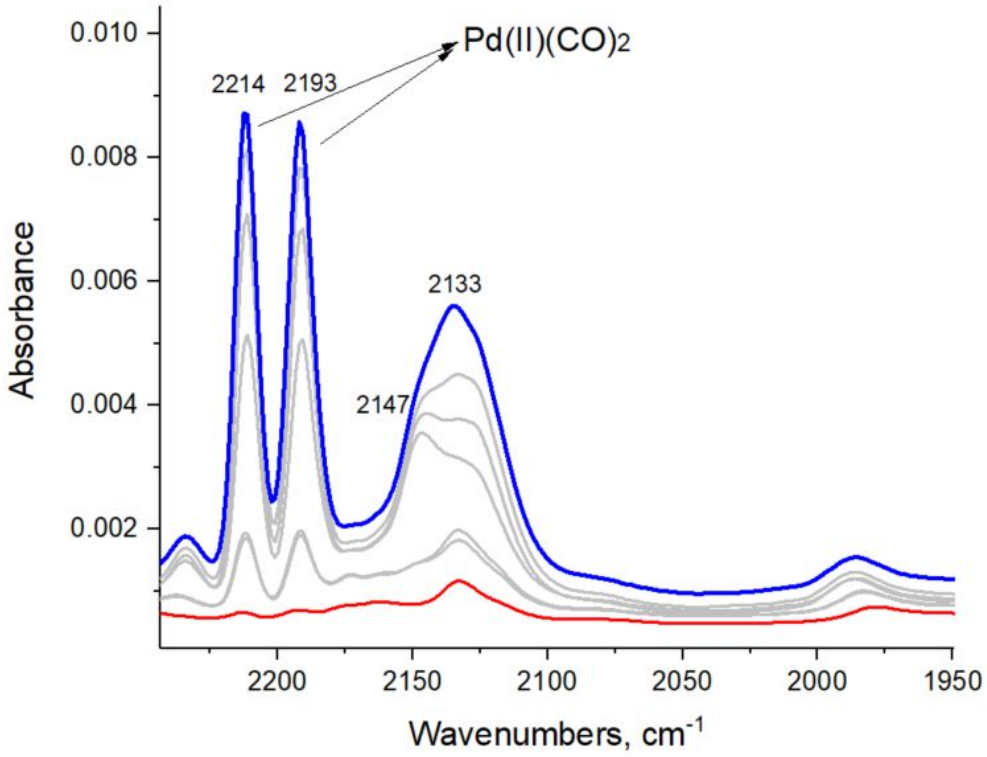

Figure S34. FTIR spectra during 5 Torr CO adsorption on 1 wt% Pd/SSZ-13 with Si/Al=12. $Pd(II)(CO)_2$ are formed with relatively high selectivity in addition to various Pd(II)(CO)(OH) species highlighting the abundance on nearby Al pairs in SSZ-13 with Si/Al ~12 (approx 3-4 Al T-sites per unit cell). Note however that for 1 wt% Pd/SSZ-13 with Si/Al 6 $Pd(II)(CO)_2$ is formed completely selectively (>95%) whereas for this sample with lower Al content a significant fraction of Pd(II)(CO)(OH) (2147-2133 cm^{-1} bands) and a minor fraction of CO adsorbed linearly on metallic Pd clusters can be seen as well. Thus, in our 1 wt% Pd/SSZ-13 with Si/Al ~6 palladium selectively goes to Pd(II)/2Al sites.

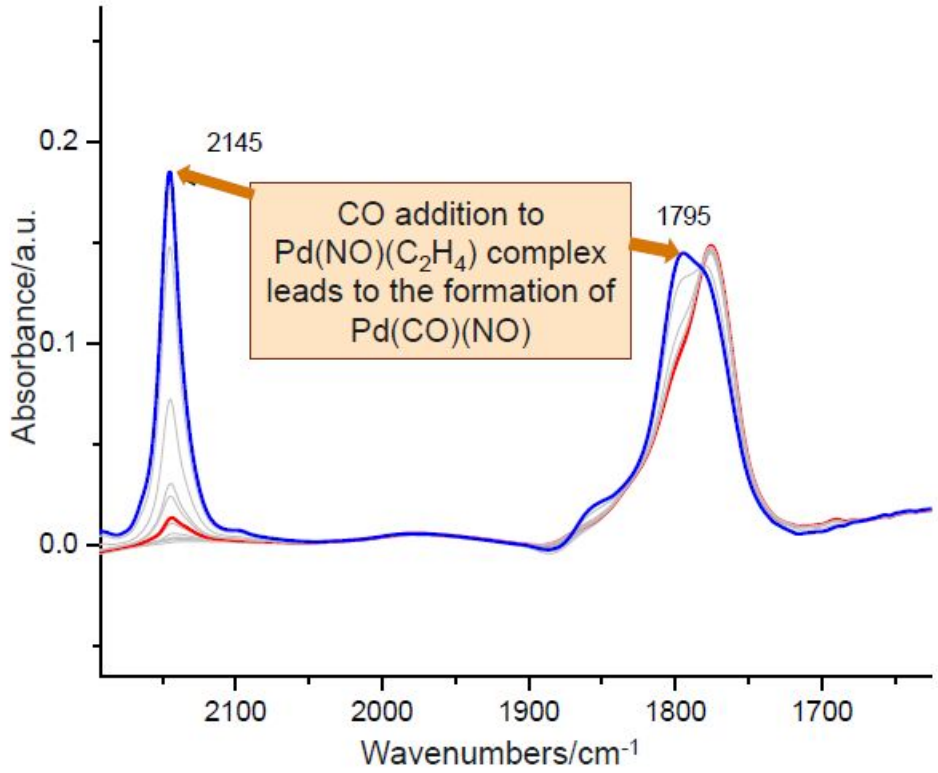

Figure S35. FTIR spectra during 0.5 Torr CO adsorption on $Pd(NO)(C_2H_4)$ complex. CO is theoretically able to react with $Pd(NO)(C_2H_4)$ the following pathways:
$Pd(NO)(C_2H_4) + CO \rightarrow Pd(CO)(C_2H_4) + NO$ ***pathway 1***
$Pd(NO)(C_2H_4) + CO \rightarrow Pd(CO)(NO) + C_2H_4$ ***pathway 2***

These data provide important information on ligand binding to Pd(II) in various mixed CO, NO and Ethylene containing Pd(II) complexes in zeolite. It is clear that pathway 2 is operative in excellent agreement with binding energies of neutral ligands obtained in our DFT calculations (***Table S1***), showing higher stability of Pd(II)(CO)(NO) compared with $Pd(II)(NO)(C_2H_4)$.

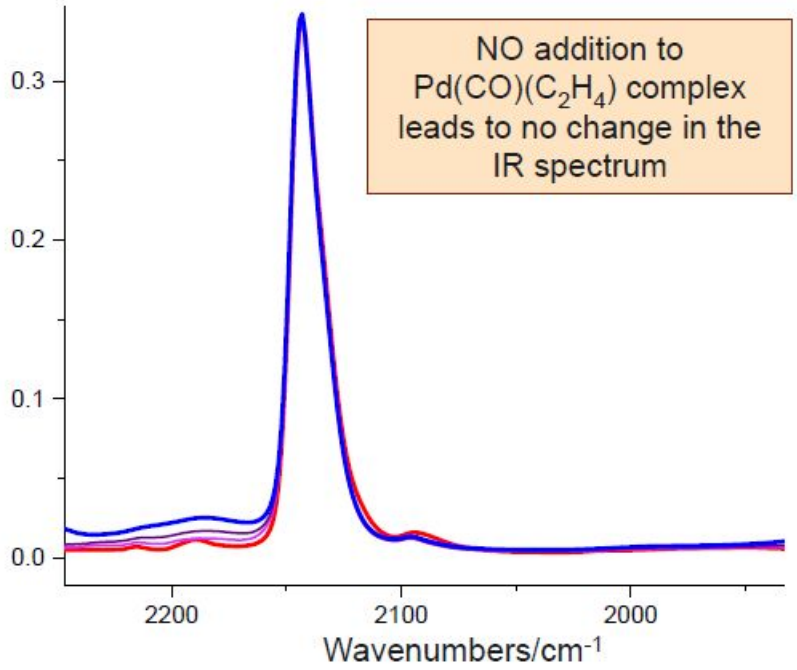

Figure S36. FTIR spectra during 0.5 Torr NO adsorption on $Pd(CO)(C_2H_4)$ complex. NO is theoretically able to react with $Pd(CO)(C_2H_4)$ the following pathways:
$Pd(CO)(C_2H_4) + NO \rightarrow Pd(NO)(C_2H_4) + CO$ ***pathway 1***
$Pd(CO)(C_2H_4) + NO \rightarrow Pd(CO)(NO) + C_2H_4$ ***pathway 2***

It is clear that $Pd(II)(CO)(C_2H_4)$ is more stable than $Pd(II)(NO)(C_2H_4)$ and Pd(II)(CO)(NO), therefore no ligand exchange takes place in agreement with our DFT calculations (***Table S1***). Thus, the row of mixed ligand binding can be constructed in terms of stability of produced complexes: $Pd(CO)(C_2H_4) > Pd(CO)(NO) > Pd(NO)(C_2H_4)$.